

Scuola di Scienze  
Dipartimento di Fisica e Astronomia  
Corso di Laurea in Astrofisica e Cosmologia

# **Giant molecular clouds properties in NGC 3627**

Relatore:

**Chiar.mo Prof. Cristian Vignali**

Correlatrice:

**Dott.ssa Rosita Paladino**

Presentata da:

**Inti Matteo Vasquez Ansaloni**

Sessione IV

Anno Accademico 2022/23

# Contents

<b>Abstract</b>	<b>3</b>
<b>Abstract (Italian)</b>	<b>5</b>
<b>1 Star Formation in Giant Molecular Clouds</b>	<b>8</b>
1.1 Interstellar medium (ISM)	9
1.2 Molecular gas	10
1.2.1 Molecular gas tracers	10
1.2.2 Conversion factor and scaling relations	11
1.3 Star formation rate tracers	12
1.3.1 H $\alpha$ observations as an indicator of SFR	13
1.4 Kennicutt-Schmidt law	14
1.5 Giant Molecular Clouds (GMC)	16
1.5.1 Influence of galactic structures on star formation and molecular clouds	17
1.5.2 Current studies	18
<b>2 ALMA and basics of interferometry</b>	<b>20</b>
2.1 Interferometry: principles and concepts	20
2.1.1 Single dish response	20
2.1.2 Aperture Synthesis	22
2.1.3 Interferometer properties	25
2.2 Calibration	26
2.2.1 $T_{\text{sys}}$ and WVR	26
2.2.2 Bandpass calibration	27
2.2.3 Time dependent calibration	28
2.2.4 Flux calibration	28
2.3 Imaging	28
2.3.1 Visibility Weighing	29
<b>3 Scientific target and observational data</b>	<b>30</b>
3.1 NGC 3627	30
3.2 ALMA Observations	32
3.3 ALMA Data reduction	34
3.3.1 CASA	34
3.3.2 Data import, inspection and flagging	34
3.3.3 A priori calibration	35
3.3.4 Bandpass calibration	35
3.3.5 Amplitude and phase vs time calibration	36

3.3.6	Inspection of calibrated data . . . . .	37
3.3.7	Imaging . . . . .	38
3.4	The moments calculation . . . . .	42
3.5	Ancillary data . . . . .	43
<b>4</b>	<b>Analysis and results</b>	<b>44</b>
4.1	Molecular gas in NGC3627 . . . . .	44
4.2	Definition of different types of environments . . . . .	45
4.3	GMCs identification . . . . .	46
4.3.1	Astrodendro . . . . .	48
4.4	Characterization of the detected GMCs . . . . .	50
4.4.1	GMC masses and mass distribution . . . . .	51
4.5	SFR . . . . .	55
4.6	Kennicutt-Schmidt Law in NGC 3627 . . . . .	56
4.7	Comparison with previous results . . . . .	58
<b>5</b>	<b>Summary</b>	<b>63</b>

# Abstract

Star formation (SF) is one of the most important processes in galaxy evolution, its physics and the deposition of mass, momentum and energy into the interstellar medium (ISM) by massive stars (‘feedback’) plays a major role in setting the structure of galaxy discs and returning material to the circumgalactic and intergalactic medium. In the nearby Universe SF occurs in the molecular component of the ISM. In the last 20 years it became clear that the key processes impacting SF occur at the interface between the kpc-scales, where gas accretion from the intergalactic medium happens, and the pc-scales, where processes such as formation of clouds and subsequent fragmentation and accretion to form denser structures, happens.

Molecular gas in galaxies is found in the form of giant molecular clouds (GMC). These clouds have been extensively studied in our Galaxy, however our position limits their view, due to line-of-sight effects. Extending this study to nearby star-forming galaxies frees us from this limitations.

Historically, observations of molecular gas in star-forming nearby galaxies were limited to global studies (at kpc scales) by limited resolution and sensitivity. The advent of ALMA revolutionized this landscape, offering unprecedented precision in studying GMCs at pc scales. The Physics at High Angular Resolution in Nearby Galaxies (PHANGS) program is a recent collaborative effort, utilizing ALMA, Hubble, JWST, and the VLT to comprehensively investigate nearby galaxies. It provides the first statistical analysis of a large sample of galaxies to gain insights into the properties of star forming-regions in different environments.

This thesis embarks on an exploration of SF processes within the barred spiral galaxy NGC 3627, focusing on the identification and characterization of GMCs across diverse galactic environments. Using ALMA CO(1-0) line emission and MUSE H $\alpha$  observations, we study the intricate relationship between molecular gas, SF rates (SFRs), and galactic structure, in the central 10 kpc region.

The integrated intensity, velocity, and velocity dispersion of the CO(1-0) line, show a rotating system with distinct SF activities in various regions. The total CO mass measured from this line amounts to  $M_{mol}^{TOT} \sim (1.6 \pm 0.2) \times 10^9 M_{\odot}$ .

We studied the molecular gas and SFR relations in different environments. We identified 552 GMCs spanning a molecular mass range of  $10^4$  to  $10^8 M_{\odot}$ , with the most massive clouds concentrated in the core. The  $M_{mol}$ -SFR relation in the whole galaxy, show a slope of  $0.83 \pm 0.04$ . We also derived the Kennicutt-Schmidt (KS) law-like relation between  $\Sigma_{M_{mol}}$  and  $\Sigma_{SFR}$ , showing a similar slope ( $N = 0.86 \pm 0.09$ ). The KS-like relations are different in different galactic environments: in the disk we measure a steep index ( $N = 1.23 \pm 0.17$ ), while in bar and bar ends we have a much flatter one. This observations suggests that there is a diversity in molecular gas and SF within the galaxy, linked to the galactic environment.

The comparison with the broader PHANGS studies reveals almost consistent results, although we use a different method of GMC identification and a different molecular gas tracer. Indeed, most of PHANGS publications are based on observations of the CO(2-1) transition, so to estimate the molecular gas mass the assumption of the line ratio CO(2-1)/CO(1-0) is needed. In this sense, observations of the CO(1-0) emission lines are extremely important, since they can provide a direct

measure of the line ratio and its spatial variation.

La formazione stellare (SF) è uno dei processi più importanti nell’evoluzione delle galassie; la sua fisica e il deposito di massa, quantità di moto ed energia nel mezzo interstellare (ISM) da parte di stelle massicce (“feedback”) giocano un ruolo fondamentale nel definire la struttura dei dischi delle galassie e nel restituire materiale al mezzo circumgalattico e intergalattico. Nell’Universo vicino, la SF avviene nella componente molecolare dell’ISM. Negli ultimi 20 anni è diventato chiaro che i processi chiave che influenzano la SF si verificano all’interfaccia tra le scale kpc, dove avviene l’accrezione di gas dal mezzo intergalattico, e le scale pc, dove avvengono processi come la formazione di nubi e la successiva frammentazione e accrezione per formare strutture più dense.

Il gas molecolare nelle galassie si trova sotto forma di nubi molecolari giganti (GMC). Queste nubi sono state ampiamente studiate nella nostra Galassia, ma la nostra posizione ne limita la visione, a causa degli effetti sulla linea di vista. L’estensione di questo studio alle galassie vicine che ospitano formazione stellare ci libera da queste limitazioni.

Storicamente, le osservazioni del gas molecolare nelle galassie vicine che ospitano formazione stellare erano limitate a studi globali (su scala kpc) a causa della risoluzione e della sensibilità limitate. L’avvento di ALMA ha rivoluzionato questo panorama, offrendo una precisione senza precedenti nello studio del GMC su scala pc. Il programma Physics at High Angular Resolution in Nearby Galaxies (PHANGS) è un recente sforzo collaborativo che utilizza ALMA, Hubble, JWST e il VLT per studiare in modo completo le galassie vicine. Il programma fornisce la prima analisi statistica di un ampio campione di galassie per comprendere le proprietà delle regioni di formazione stellare in ambienti diversi.

Questa tesi intraprende un’esplorazione dei processi di SF all’interno della galassia a spirale barrata NGC 3627, concentrandosi sull’identificazione e la caratterizzazione delle GMC in diversi ambienti galattici. Utilizzando l’emissione della linea CO(1-0) di ALMA e le osservazioni *Halfa* di MUSE, studiamo l’intricata relazione tra gas molecolare, tassi di SF (SFR) e struttura galattica, nella regione centrale di 10 kpc.

L’intensità integrata, la velocità e la dispersione di velocità della linea del CO(1-0) mostrano un sistema rotante con attività di SF in varie regioni. La massa totale di CO misurata da questa linea ammonta a  $M_{mol}^{TOT} \sim (1,6 \pm 0,2) \times 10^9 M_{\odot}$ .

Abbiamo studiato le relazioni tra gas molecolare e SFR in diversi ambienti. Abbiamo identificato 552 GMC che coprono un intervallo di massa molecolare compreso tra  $10^4$  e  $10^8 M_{\odot}$ , con le nubi più massicce concentrate nel nucleo. La relazione  $M_{mol}$ -SFR nell’intera galassia, mostra una pendenza di  $0,83 \pm 0,04$ . Abbiamo anche derivato la relazione simile alla legge di Kennicutt-Schmidt (KS) tra  $\Sigma_{M_{mol}}$  e  $\Sigma_{SFR}$ , che mostra una pendenza simile ( $N = 0,86 \pm 0,09$ ). Le relazioni simil-KS sono diverse nei vari ambienti galattici: nel disco misuriamo un indice ripido ( $N = 1,23 \pm 0,17$ ), mentre nella barra e nelle estremità della barra abbiamo un indice molto più piatto. Queste osservazioni suggeriscono che esiste una diversità di gas molecolare e SF all’interno della galassia, legata all’ambiente galattico.

Il confronto con gli studi più ampi di PHANGS rivela risultati quasi del tutto coerenti, anche se utilizziamo un metodo diverso di identificazione del GMC e un diverso tracciante del gas molecolare. Infatti, la maggior parte delle pubblicazioni di PHANGS si basa su osservazioni della transizione

CO(2-1), quindi per stimare la massa del gas molecolare è necessaria l'assunzione del rapporto tra le linee CO(2-1)/CO(1-0). In questo senso, le osservazioni delle righe di emissione della CO(1-0) sono estremamente importanti, poiché possono fornire una misura diretta del rapporto di righe e della sua variazione spaziale.

# Chapter 1

## Star Formation in Giant Molecular Clouds

Understanding star formation (SF) mechanisms within galaxies is one of the most fundamental issues in the field of the formation of galaxies and its evolution over time. The physics of star formation and the deposition of mass, momentum and energy into the interstellar medium by massive stars (‘feedback’) plays a major role in setting the structure of galaxy discs and returning material to the circumgalactic and intergalactic medium. Moreover, feedback processes are the main uncertainties in modern cosmological simulations of galaxy formation and evolution [33].

SF is a complex process that involves a diverse range of physical phenomena. Research over the last 20 years has revealed that the rate of large-scale star formation is influenced by both macro-level physical processes, such as gas accretion onto disks from satellite objects and the intergalactic medium, as well as micro-level processes that occur on cloud scales. These micro-level processes include gas cooling on kiloparsec scales, the formation of molecular clouds on parsec scales, and the subsequent fragmentation and accretion of this molecular gas to form denser structures [18]. The key processes that impact SF occur at the interface between these physical scales.

The SF process requires the presence of gas cold enough to collapse. The cold phases of the Inter-Stellar Medium (ISM) are the only ones that can accommodate these phenomena, and in particular, in the local Universe, it is the molecular component of the ISM that hosts SF.  $\text{H}_2$  is the most abundant molecule in the Universe and the dominant component of the molecular ISM. However, due to its high excitation temperatures, it is virtually invisible in the radio and very difficult to observe in the UV. In order to detect this gas, it is therefore necessary to observe other more easily excitable molecules that serve as tracers. Because of its abundance and properties (dipole and moment of inertia), the CO molecule turns out to be an excellent tracer for molecular gas, detectable in the millimeter band.

Molecular gas in galaxies is found in the form of clouds or clumps. These clouds have been extensively studied in our Galaxy, even to the point of establishing empirical scaling relationships linking the various properties of these clouds [35]. However, our position in the Milky Way limits our view of these structures. Thus, there is a need to pursue observations of molecular gas in nearby star-forming galaxies, particularly of the larger and more massive molecular clouds known as Giant Molecular Clouds (GMCs). GMCs serve as the primary sites for star formation and set the boundary conditions for this process [31].

In the past, CO emission maps in massive star-forming spiral galaxies where individual GMCs could be well distinguished were rare due to the limited resolution and sensitivity of available millimeter-wave telescopes (e.g. CANON Survey [42]; The PdBI (Plateau de Bure Interferometer)

Arcsecond Whirlpool Survey (PAWS) [57]). The ALMA telescope offered us the opportunity to change this situation; thanks to its unprecedented resolution, it allowed us to study GMCs (and star-forming regions in general) in star-forming galaxies with unprecedented precision.

In this thesis, we use ALMA data to study the barred spiral galaxy NGC 3627. Barred spirals offer the opportunity to study GMCs and SF in a wide variety of environments, from disc and spiral arms, to the bar, the bar ends and the nucleus. The need to study the SF in different environments is due to the fact that it can vary dramatically from one environment to another [24] [27] [14] [54]. Our work has focused on identifying and characterizing the GMCs of this galaxy in its different environments, and then relating them to the SF levels.

Our available data consisted of 3 datasets of ALMA observations of CO(1-0) line, which allowed us to achieve an angular resolution of 1.6 arcsec, suitable for resolving individual clouds. Also, we used MUSE observations of H $\alpha$  (at a resolution of 1.05 arcsec) to determine star formation rates (SFRs).

## 1.1 Interstellar medium (ISM)

The interstellar medium (ISM) refers to the plasma contained within galaxies, consisting of gas and dust. The ISM bears the mark of various processes that have influenced and continue to influence a specific galaxy, such as pressure, turbulence, presence of magnetic fields, depletion by star formation and black holes, heating and feedback from supernova explosions, and accretion from the intergalactic medium, circumgalactic medium, and interactions with other galaxies [58].

The ISM encompasses a wide range of temperature and density, spanning over six orders of magnitude. Pressure equilibrium governs its behavior, leading to its division into three distinct phases [41][16]: the hot ionized medium (HIM); the warm medium, including both a neutral (WNM) and an ionized (WIM) component; and the cold neutral medium (CNM). In galaxies like the Milky Way, the HIM and medium WIM occupy the majority of the volume. However, despite their dominance in volume, their low densities (around  $10^{-3}$  to  $10^{-1} \text{cm}^{-3}$ ) mean that the cooler and denser neutral phases contain most of the mass [19].

In a typical nearby star-forming late-type galaxy, the CNM makes up approximately 10-20% of the total baryonic mass, which includes both gas and stars. Within this cold ISM, about 75% of the mass consists of atomic gas, primarily hydrogen (H). This atomic gas exists in two distinct phases: a warm phase at around 5,000 K with a density of approximately  $0.6 \text{cm}^{-3}$ , and a colder, denser phase at around 100 K with a density of approximately  $30 \text{cm}^{-3}$ . Both of these phases contribute to the observed emission in the hyperfine transition of HI (observed at 21cm) [19]. The remaining 25% of the mass is in the **molecular form**, with temperatures ranging from  $\sim 10\text{K}$  to  $100\text{K}$  and densities of  $\sim 10^3 - 10^6 \text{cm}^{-3}$ . The dust amounts to 1% of the total gas mass and it is present in both the atomic and molecular regions, making it a tracer of the overall gas distribution profile [55].

The scenario for early-type galaxies is quite distinct, as the CNM only contributes to less than 3% of the total baryonic mass, and the rest of the medium is in the HIM phase. In cases where molecular gas is present, it typically exhibits central concentration within a disk characterized by a small scale length. However, despite this, the gas can still possess central surface densities comparable to those found in late-type galaxies [17]. The star formation in these galaxies is notably scant in comparison to that observed in the late-type counterparts.

## 1.2 Molecular gas

In essence, the process of star formation hinges on the presence of sufficient cold gas capable of gravitational collapse. Given this requirement, the cold phases of the ISM emerge as the only plausible sites for stars to come into being. As a result, quantifying the available gas for star formation in galaxies across different cosmic eras becomes pivotal for understanding how galaxies have evolved over time.

Zooming in on our local Universe, we find that all star formation takes place exclusively within the molecular ISM, where molecular hydrogen ( $\text{H}_2$ ) stands as the primary fuel for this process. Of particular note are the molecular clouds, which constitute the coldest (with temperatures around  $\sim 10$  K in the absence of star formation) and densest (with particle densities exceeding  $30 \text{ cm}^{-3}$ ) regions of the ISM[31]. These molecular clouds, given their unique properties, serve as the most favorable settings for star formation to occur. Molecular clouds are the central topic of this work and will be discussed in detail later.

### 1.2.1 Molecular gas tracers

$\text{H}_2$  is the most abundant molecule in the Universe. In the present-day Universe, the formation of  $\text{H}_2$  molecules primarily occurs on dust grain surfaces. Due to its high sensitivity to UV radiation, the formation of molecular hydrogen requires extinctions of at least  $A_V \gtrsim 1$  (where  $A_V$  is the extinction measured in the V band<sup>1</sup>)[2].

Despite its high abundance, due to the high temperatures required for its excitation ( $\sim 100$  K),  $\text{H}_2$  is not observable in the radio and is difficult to observe in the UV. Fortunately, where we have  $\text{H}_2$ , we also have carbon monoxide (CO). The CO molecule constitutes the second most abundant molecule after molecular hydrogen. It has a permanent dipole moment and a much higher moment of inertia than  $\text{H}_2$ . Consequently, CO has low energy rotational transitions, leading to excitation and detectable emission at low temperatures. Hence, in particular, at low temperatures ( $T \sim 10$  K) and number densities above  $n_{\text{H}} \sim 10^2 \text{ cm}^{-3}$ , CO is regularly used as an effective tracer of the molecular ISM, since its primary source of excitation is collisions with  $\text{H}_2$  [8], therefore it is widely used to measure molecular gas masses. Moreover, the  $J = 1 \rightarrow 0$  transition of  $^{12}\text{CO}$  falls within a relatively transparent atmospheric window at a wavelength of 2.6 mm. As a result, this molecular transition has become the primary tool for tracing the overall distribution of  $\text{H}_2$  in our Galaxy and beyond. The standard methodology posits a simple relationship between the observed CO intensity and the column density of molecular gas, such that [7]:

$$N(\text{H}_2) = X_{\text{CO}} W(^{12}\text{C}^{16}\text{O}; J = 1 \rightarrow 0) \quad (1.1)$$

where the column density,  $N(\text{H}_2)$ , is in  $\text{cm}^{-2}$  and the integrated line intensity,  $W(\text{CO})$ , is in  $K \text{ km/s}$ .  $X_{\text{CO}}$  represents a conversion factor.

From integrating over the emitting area and correcting by the mass contribution of heavier elements mixed in with the molecular gas, we can find the total molecular mass:

$$M_{\text{mol}} = \alpha_{\text{CO}} L_{\text{CO}} \quad (1.2)$$

where  $M_{\text{mol}}$  is expressed in solar masses.  $L_{\text{CO}}$  is the luminosity of the CO line, related to the observed integrated flux density in galaxies; it is usually expressed in  $[K \text{ km/s pc}^2]$  and is given by:

$$L_{\text{CO}} \approx S_{\text{CO}} \Delta\nu \frac{D_L^2}{1+z} \quad (1.3)$$

---

<sup>1</sup> $E(B - V) = (B - V) - (B - V)_o \rightarrow A_V = 3.2E(B - V)$

where  $S_{CO}\Delta\nu$  is the integrated line flux density (in  $Jy\ km/s$ ),  $D_L$  is the luminous distance (in Mpc) and  $z$  is the redshift. The factor  $\alpha_{CO}$  in (1.2) acts as a mass-to-light ratio.

Both  $X_{CO}$  and  $\alpha_{CO}$  are referred as the CO-to- $H_2$  conversion factor. For  $X_{CO} = 2 \times 10^{20}\ cm^{-2}\ (K\ km/s)$ , the correspondent mass-to-light ratio is  $\alpha_{CO} = 4.3 M_\odot (\frac{km}{s\ pc})^{-1}$ . To translate integrated flux directly to molecular mass, equation (1.2) can be written as:

$$M_{mol} = 1.05 \times 10^4 \left( \frac{X_{CO}}{2 \times 10^{20} \frac{cm^{-2}}{K\ km/s}} \right) \frac{S_{CO}\Delta\nu D_L^2}{(1+z)} M_\odot \quad (1.4)$$

## 1.2.2 Conversion factor and scaling relations

### $\alpha_{CO}$ conversion factor

Due to the typically optically thick nature of the  $^{12}CO(J = 1 \rightarrow 0)$  transition, its brightness temperature is associated with the temperature of the surface rather than the column density of the gas. Information regarding the mass of a self-gravitating entity, like a molecular cloud, is conveyed through its line width, reflecting the velocity dispersion of the emitting gas. For virialized molecular clouds, where twice the internal kinetic energy equals the potential energy, the virial mass  $M_{vir}$  is given by (taken from [7]):

$$M_{vir} = \frac{3(5-2k)}{G(3-k)} R\sigma^2 \quad (1.5)$$

where  $R$  is the projected radius (in pc),  $\sigma$  is the 1D velocity dispersion (in km/s;  $\sigma_D = \sqrt{3}\sigma$ ),  $G$  is the gravitational constant ( $G \approx \frac{1}{232} M_\odot^{-1}\ pc\ km^2\ s^{-2}$ ), and  $k$  is the power-law index of the spherical volume density distribution:  $\rho(r) \propto r^{-k}$ , and is typically taken as  $k = 1$ .

This virial mass estimate remains robust unless other terms, such as magnetic support, can be neglected[3]. As long as molecular gas dominates the mass within the cloud radius and the cloud is approximately virialized,  $M_{vir}$  serves as a reliable measure of the  $H_2$  mass.

It has been empirically observed that molecular clouds follow some scaling relationships (the so-called Larson's Laws). Specifically, molecular clouds exhibit a size-line-width relation given by:

$$\sigma = CR^a \quad (1.6)$$

where the canonical value of the power index is  $a \approx 0.5$  and  $C \approx 0.7\ km\ s^{-1}\ pc^{-0.5}$ .

By combining equations 1.5 and 1.6, we can see that:

$$M_{vir} \propto \sigma^4 \quad (1.7)$$

and clouds that fulfill these two equations will have a surface density that depends on the coefficient in equation 1.6:

$$\Sigma_{cloud} = \frac{M_{vir}}{\pi R^2} \propto C^2. \quad (1.8)$$

Since the brightness of a cloud is the product of its area ( $\pi R^2$ ) and its integrated surface brightness ( $T_B \sqrt{2\pi}\sigma$ ), then:

$$L_{CO} = \sqrt{2\pi^3} T_B \sigma R^2, \quad (1.9)$$

where,  $T_B$  is the Rayleigh-Jeans brightness temperature of the emission<sup>2</sup>

Combining Eq. 1.6 and Eq. 1.9, we get that:  $L_{CO} \propto T_B \sigma^5$ . Using the relationships found, and assuming that clouds are virialized, we can begin to relate mass to luminosity:

$$M_{vir} \approx M_{mol} \approx 200 \left( \frac{C^{1.5} L_{CO}}{T_B} \right)^{0.8} \quad (1.10)$$

Then, using Eq. 1.8, we find the following expression for the conversion factor:

$$\alpha_{CO} \equiv \frac{M_{mol}}{L_{CO}} \propto L_{CO}^{-0.2} T_B^{-0.8} \Sigma_{cloud}^{0.6} \quad (1.11)$$

The latter expression has certain assumptions:

1. Clouds are virialized,
2. The mass of a cloud is dominated by  $H_2$ ,
3. Cloud masses follow the trend given by the equation 1.6,
4. Clouds have a nearly constant temperature over their entire surface.

The in-depth study of molecular clouds allows for better constraints on the conversion factor. Studying the dynamics of these clouds, especially the comparison and relationship between  $M_{vir}$  and  $M_{CO}$ , provides independent evidence for the CO-to- $H_2$  conversion factor that one uses.

### $X_{CO}$ conversion factor

While the emission from the  $^{12}CO(J = 1 \rightarrow 0)$  transition is usually optically thick, circumstances like highly turbulent gas motions or significant velocity dispersions (e.g., stellar outflows and possibly galactic winds) can render the emission optically thin. Consequently, it is worthwhile to contemplate the optically thin limit concerning the CO-to- $H_2$  conversion factor, which is related to the column density and the integrated intensity of the transition:

$$X_{CO} = \frac{N(H_2)}{W(CO)} \approx 1.6 \times 10^{19} \frac{T_{ex}}{30K} e^{\frac{5.53K}{T_{ex}} - 0.184} [cm^{-2} (km/s)^{-1}] \quad (1.12)$$

## 1.3 Star formation rate tracers

The rate (per year) at which gas and dust within a galaxy (or a specific region of it) are converted into stars is called Star Formation Rate (SFR). SFRs, along with masses, are among the most important parameters that define galaxies and their evolution throughout cosmic times. There is a wide range of techniques used to measure the rate of star formation, depending on whether the target is resolved into individual units (such as young stars) or not. However, the first step in understanding whether there is star formation is to identify the emission that probes newly or recently formed stars, while avoiding as much as possible contributions from evolved stellar populations. [10].

---

<sup>2</sup>In the case of a  $J \rightarrow J - 1$  transition, it is given by:  $T_J \approx 5.53J(1 - e^{-\tau J} (\frac{1}{e^{\frac{5.53J}{T_{ex,J}} - 1}} - \frac{1}{e^{2.73(z+1)} - 1}}))$  [Kelvin], where  $T_{ex,J}$  refers to the excitation temperature, which is defined as the temperature required to restore the relative populations of the  $J$  and  $J - 1$  levels according to the Boltzmann distribution.

The definition of “recent” varies depending on the application and system being studied. For whole galaxies, most researchers agree that “recent” refers to timescales of approximately 10-100 million years, while for regions or structures within galaxies such as giant molecular clouds, it refers to timescales of approximately 1-10 million years [10].

To measure SFRs in resolved regions like those within the Milky Way, the most common method is to count individual objects or events that indicate recent star formation, such as supernovae [13]. In molecular clouds located within 0.5-1 kiloparsec of the solar system, this is achieved by counting young stellar objects (YSOs), which are protostars at various stages of development. These YSOs are best identified in the infrared since they are still enclosed within their original clouds.

In unresolved systems, SFR indicators are merely measures of luminosity, which can be either monochromatic or integrated over a certain wavelength range. The purpose of these measures is to target continuum or line emission that is sensitive to the short-lived massive stars. To convert the luminosity of massive stars to a SFR, certain assumptions are made. These include:

1. The SFR has remained relatively constant over the timescale being studied by the specific emission being used.
2. The initial mass function (IMF) of the stars is either known or can be controlled, allowing for the extrapolation of the number of massive stars to the total number of high and low mass stars formed.
3. The IMF is fully sampled, meaning that at least one star is formed in the highest-mass bin, and all other mass bins are populated accordingly with one or more stars.

SFR indicators can be categorized into two types based on the wavelength range they operate in. The first type, which operates in the UV/optical/near-IR range ( $\sim 0.1\text{-}5\ \mu\text{m}$ ), probes the direct stellar light that emerges from galaxies. The second type, which operates in the mid/far-IR range ( $\sim 5\text{-}1000\ \mu\text{m}$ ), probes the stellar light that has been reprocessed by dust.

### 1.3.1 $H\alpha$ observations as an indicator of SFR

In addition, the ionizing photon rate, which is traced by the gas ionized of massive short-lived stars (O and B-type), can also be used to define SFR indicators both within and beyond our galaxy. The production of ionizing photons by young, massive stars results in the ionization of the surrounding gas. This ionization process triggers hydrogen recombination cascades, which generate line emission, including the Balmer series lines of  $H\alpha$  ( $0.6563\ \mu\text{m}$ ) and  $H\beta$  ( $0.4861\ \mu\text{m}$ ). These lines are considered the most conventional indicators of SFR due to their strength and location within the optical wavelength range ([29]).

To measure the SFR from  $H\alpha$  observations, a calibration that relates the  $H\alpha$  luminosity to the SFR is used. This calibration is based on theoretical models of the ionized gas in star-forming regions and empirical measurements of the SFR in nearby galaxies. Only stars with masses  $>10\ M_{\odot}$  and lifetimes  $<20\ \text{Myr}$  contribute significantly to the integrated ionizing flux, so the emission lines provide a nearly instantaneous measure of the SFR, independent of the previous star formation history. For solar abundances and assuming Salpeter IMF ( $0.1\text{-}100\ M_{\odot}$ ), the calibration of SFR is given by ([67]; [38]):

$$SFR(M_{\odot}yr^{-1}) = 7.9 \times 10^{-42} L(H\alpha)(erg/s) \quad (1.13)$$

where  $L(H\alpha)$  is the luminosity of  $H\alpha$  line. Equation (1.13) is computed considering an electron temperature  $T_e=10000\ \text{K}$ .

SFR indicators that use hydrogen ionization to track the formation of massive stars are susceptible to the influence of dust. The most commonly treated effect is that of dust attenuation of the line or continuum. It is worth mentioning that the impact of dust attenuation decreases with increasing wavelength. The emergence of new or significantly enhanced radio and millimeter facilities, such as ALMA or VLA (the Karl G. Jansky Very Large Array), has opened up opportunities to explore millimeter and/or radio recombination lines as alternative methods for measuring SFRs without being affected by dust attenuation. However, these methods rely on lines that are inherently very weak ([10]).

## 1.4 Kennicutt-Schmidt law

It is useful to relate the two notions previously discussed (i.e. the amount of gas in a galaxy or its substructure and the SFR) in order to define a SF law and to understand, in a tangible manner, whether and how the amount of gas in a Galaxy influences its evolution. When plotting the surface densities of star formation rate ( $\Sigma_{SFR}$ ) against the mean gas surface densities ( $\Sigma_{gas}$ ), a remarkably tight scaling law is observed [29]. This correlation highlights the fact that gas serves as the driving force for star formation. Additionally, it suggests that star formation is more efficient when there are higher gas densities. The concept of a power-law relation between SFR density and gas density can be traced back to Schmidt (1959, 1963), formulated in the shape of a power-law (the so-called Schmidt law):

$$\rho_{SFR} = (\rho_{HI})^n \quad (1.14)$$

where  $\rho_{SFR}$  is the SFR per unit volume and  $\rho_{HI}$  is the HI volume density (when this correlation was first identified, was not possible to observe molecular gas emission). By analyzing the distribution of young stars within the Milky Way, Schmidt proposed that the exponent ‘n’ of this power law falls within the range of 2 to 3.

When we focus on galaxies beyond the Milky Way, our direct observations are limited to projected quantities, such as surface densities. Hence, the commonly used relation, known as the Kennicutt-Schmidt (KS) law, is expressed in terms of surface densities[31]:

$$\Sigma_{SFR} \propto (\Sigma_{gas})^N \quad (1.15)$$

where N is usually called Schmidt index or KS index. The value of N varies depending on the type of galaxy and the tracer used to measure the gas density. The present configuration of KS law was examined in a comprehensive study of 100 galaxies by Kennicutt (1998)[30], revealing a remarkably strong non-linear correlation with a Schmidt index  $N \sim 1.4$  for total gas (atomic plus molecular), while  $N \sim 1$  for molecular gas. This KS law appears to maintain a similar N value across a broad range of redshifts and environments[31]. An example of this relationship is shown in Figure 1.1.

A physical interpretation for this empirically derived law is that a consistent fraction of the gas within molecular clouds (with a density  $\rho_{gas}$ ) undergoes star formation at each free-fall time ( $t_{ff}$ ). So, the density of SFR will be:

$$\rho_{SFR} \propto \rho_{gas}/t_{ff} , \quad (1.16)$$

whit:

$$t_{ff} \propto \sqrt{1/\rho_{gas}} \quad (1.17)$$

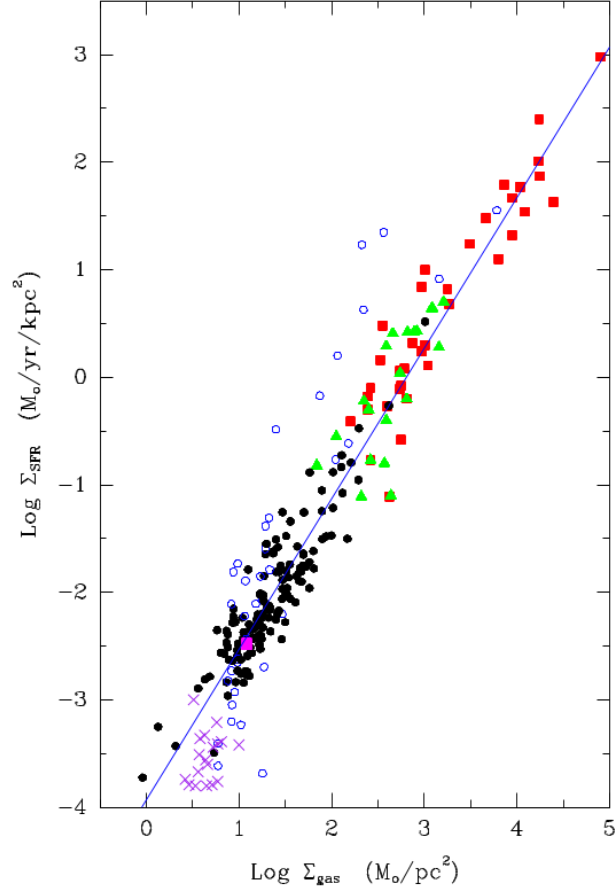


Figure 1.1: between the surface densities of star formation and gas (both atomic and molecular) averaged across the disk, categorized by different classes of star-forming galaxies. Each data point corresponds to an individual galaxy, with the SFR and gas masses normalized to the radius of the primary star-forming disk. The line overlays the data, depicting the original  $N = 1.4$  fit derived by Kennicutt (1998b). [31]

$$\rightarrow \rho_{SFR} \propto \rho_{gas}^{3/2} \rightarrow \Sigma_{SFR} \propto \Sigma_{gas}^{3/2} \quad (1.18)$$

Hence, this interpretation produces an index  $N=1.5$ . [20][39].

An alternative perspective suggests that the SFR is dictated by the quantity of dense molecular gas, resulting in a linear star formation law when the dense gas fraction remains constant. This notion is supported by an examination of the connection between integrated SFRs and dense molecular gas masses, as determined through HCN  $J = 1 \rightarrow 0$  measurements, in a collection of normal and starburst galaxies[65]. Unlike the correlation observed with the overall molecular mass derived from CO, this relationship exhibits linearity, indicating a robust association between the masses of dense molecular clumps and the formation of stars [34]. Remarkably, this connection appears to be largely unaffected by the specific star-forming environment within the galaxy.

Under this interpretation, the reason behind the linear correlation between SFR and HCN luminosity in galaxies is that the measurement of HCN luminosity essentially quantifies the number of these dense structures within a galaxy. Each of these structures has a relatively roughly fixed

SFR, regardless of the galactic environment in which it exists.

### Spatially resolved KS Law in galaxies

To gain a deeper understanding of the mechanisms behind this observed law, further investigation at a smaller (cloud) scale – specifically at a sub-kpc level – is necessary. However, the findings at these scales have not yet provided conclusive results. For example, Onodera et al. 2010 [46] conducted observations of the M33 galaxy in the  $^{12}\text{CO } J = 1 \rightarrow 0$  transition at a high spatial resolution ( $\sim 80$  pc). Their findings revealed that the surface densities of SFR and molecular gas exhibit a strong correlation only up to scales of  $\sim 1$  kpc. At smaller scales, this correlation is no longer observed. On the other hand, Williams et al. 2018 [64] conducted observations of the same galaxy using the  $^{12}\text{CO } J = 2 \rightarrow 1$  transition. The results of their study demonstrated that the correlation between the surface densities of SFR and molecular gas persists even at small scales ( $\sim 100$  pc).

These opposite results may arise from the different assumptions made during the calculation of the SFR, as well as the choice of tracer used. The 2-1 transition, for instance, traces warmer and denser gas, which is more likely to be associated with star formation.

When focusing on the dense gas fraction, it has been observed that the SFRs and total molecular masses, from local cloud scales to galaxy scales, show a correlation over a large mass range, as shown in Figure 1.2 (take from [34]). This relationship is captured by a family of linear star formation scaling laws, parameterized by  $f_{DG}$ , which emphasizes the dense gas fraction:

$$\Sigma_{SFR} \propto f_{DG} \Sigma_{H_2} \quad (1.19)$$

In other words, the underlying star formation scaling law is consistently linear for clouds and galaxies with the same dense gas fraction. These findings provide a unified framework for understanding the relationship between the standard (non-linear) extragalactic Schmidt-Kennicutt scaling law, typically derived from CO observations of the gas, and the linear star formation scaling law derived from HCN observations of the dense gas [34].

## 1.5 Giant Molecular Clouds (GMC)

The molecular CNM plays a fundamental role in star formation, as it has the right temperatures to allow gas aggregation and its gravitational collapse. This kind of ISM appears in the form of gravitationally bound clouds (*molecular clouds*) and is primarily located in areas where stars are formed (i.e. the spiral arms and regions where matter is condensed due to interactions).

Molecular clouds with masses of about  $10^4 - 10^7 M_{\odot}$  and sizes of about 10-100 pc [14] are called **Giant Molecular Clouds** (GMC) and may contain several sites of star formation [63].

As we anticipated in section 1.2.2, it has been empirically shown that molecular clouds (which we can now identify with the label GMC) tend to follow scaling relationships (*Larson's Law*). In addition to the relationship given in Equation 1.6, there are these others:

$$M \propto R^b \quad (1.20)$$

$$\sigma \propto (R\Sigma)^c \quad (1.21)$$

with their canonical power indexes:  $b \approx 2$  and  $c \approx 0.4$ . These relationships imply a constant surface density.

In star forming galaxies, the process of star formation is often considered to be localized: the coldest gas within GMCs collapses to form stars in cores that are much smaller in size (at least one

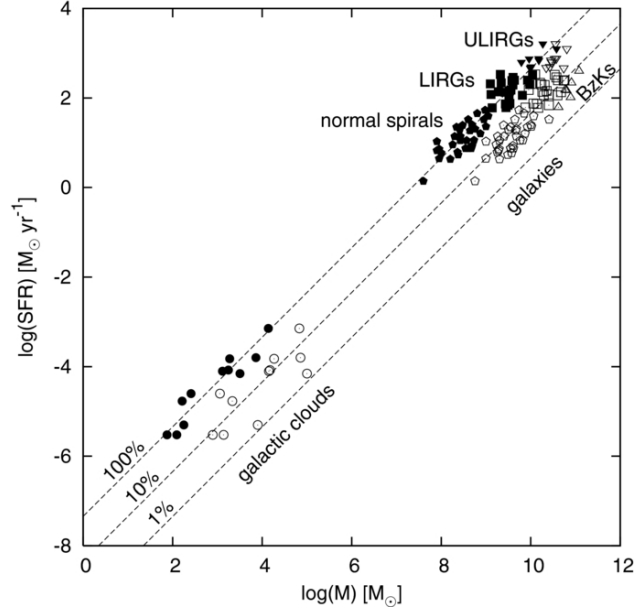


Figure 1.2: SFR–molecular-mass diagram illustrating data from the Gao & Solomon (2004a) sample, including both local molecular clouds and galaxies. Solid symbols indicate measurements of dense cloud masses, derived from either extinction observations for galactic clouds or HCN observations for galaxies. Open symbols represent measurements of total cloud masses for the same clouds and galaxies, obtained from either extinction measurements (for galactic clouds) or CO observations (for galaxies). In the case of galaxies, normal spirals are denoted by pentagons, starburst galaxies by squares (LIRGs), and inverted triangles (ULIRGs). High-redshift BzK galaxies are represented by triangles. SFRs for the Gao and Solomon galaxies have been adjusted upward by a factor of 2.7 to align with those of galactic clouds when extrapolated to local cloud masses. [34]

order of magnitude smaller than the GMC and three orders of magnitude smaller than a typical galaxy). The rate at which stars form is determined by the properties of GMCs such as their level of turbulence, chemical composition, strength and structure of magnetic fields, or the flux of cosmic rays [37] [40].

However, it is worth noting that the evolution of GMCs may also be influenced by larger-scale dynamics. Galactic processes, such as spiral density waves, interactions with other galaxies, and the influence of the galactic magnetic field, can affect the overall structure and stability of GMCs. Additionally, feedback from massive stars (e.g. photoionisation, stellar winds, and supernovae) plays a crucial role in regulating star formation within GMCs and eventually contributes to dispersing the parent cloud [12].

### 1.5.1 Influence of galactic structures on star formation and molecular clouds

Describing the properties of GMCs is a complex task. While some observations and theoretical simulations suggest that GMCs exhibit global similarities across different galaxies, regardless of the galaxy’s specific characteristics [23], other research has shown that the properties of GMCs are influenced by the type and morphology of the galaxy, as well as environmental factors. These variations can result in differences in the SFR from case to case and deviations from the Kennicutt-Schmidt law.

Recent studies on extra-galactic GMCs at a cloud-scale have revealed that these clouds exhibit a

wide range of physical properties, including surface density and dynamical state. Various environmental factors, such as galactic shear, differential non-circular motions, gas flows along and through stellar dynamical structures (such as bar and spiral arms [25]), and accretion flows, play a crucial role in determining which pockets of the GMCs collapse and when. Theoretical studies suggest that these mechanisms operate on different timescales, leading to variations in the star formation process from galaxy to galaxy and within a galaxy. Therefore, to gain a comprehensive understanding of how star formation works in galaxies, it is essential to have a large sample size that covers a range of galactic environments and ISM properties and conditions ([47]).

The conventional perspective on the evolution of GMCs in spiral arm environments suggests that their development is affected by “galactic shock” caused by quasi-stationary density waves. When gas flows across a spiral arm, it undergoes sudden compression due to the galactic shock, leading to cloud formation during a phase transition. The incoming clouds are then shock-compressed and undergo gravitational collapse, which triggers star formation. This scenario predicts that GMCs follow evolutionary sequences across spiral arms in a broad radial range, as observed in recent studies of GMCs in nearby spiral galaxies like M51 and IC 342 ([1]).

In the bar, the situation regarding star formation is often unclear, with instances of a complete lack of SF [28]. This may be due to the presence of non-circular motions that induce shear motions. These shear motions can stabilize the clouds and prevent them from collapsing.

In this sense, the regions where galactic bars and spiral arms intersect are of great interest as they are some of the most active star-forming areas in the local Universe. In the Milky Way, the overlap between the end of the Galactic bar and the inner Scutum-Centaurus spiral arm is home to the W43 mini-starburst ([43], [4], and [50]). However, it is still unclear whether the enhanced star formation in this region is due to the build-up of locally high gas densities or collisions between gas clouds. One peculiar aspect of W43 is that two prominent velocity components along the line of sight, separated by 50 km/s, may both be spatially associated with this region and even interact. Unfortunately, due to our position in the Galaxy, it is currently impossible to determine whether the two gas components are indeed interacting or just chance alignments in different parts of the Galaxy.

To understand the structure of GMCs and the processes that lead to SF and influence it, a parsec-scale study of clouds in the extragalactic environment is necessary. However, in the past years, the sensitivity and resolution limitations of millimeter-wave telescopes have resulted in only a few exceptions where maps of CO emission in massive star-forming spiral galaxies can distinguish individual GMCs. ALMA has the potential to change this situation by offering unprecedented sensitivity and the ability to resolve star-forming structures in external galaxies in a reasonable amount of time.

### 1.5.2 Current studies

The Physics at High Angular Resolution in Nearby Galaxies (PHANGS) program<sup>3</sup> stands out as a leading initiative in GMC research, fostering collaboration across diverse space- and ground-based telescopes such as ALMA, Hubble, JWST, and the VLT. This extensive effort is designed to comprehensively study a significant number of nearby galaxies with high resolution. The primary focus is on unraveling the intricacies of the star formation cycle, including aspects like GMC collapse and feedback processes. A crucial aspect of PHANGS is its emphasis on statistical analysis, leveraging the galactic sample to gain insights into the statistical properties of these galaxies and their star-forming regions. This statistical approach enhances our understanding of the small-

<sup>3</sup><https://sites.google.com/view/phangs/home>

scale gas physics, galactic structure, and overall galaxy evolution in the context of nearby massive star-forming galaxies.

In this context, works such as Sun, 2018 [59] have studied the dynamical properties of GMCs (in particular the  $\sigma$  velocity dispersion) and linked them to their surface densities from ALMA CO(2-1) observations. The results show a correlation between  $\sigma$  and  $\Sigma$  and a large variation of the turbulence pressure ( $P_{turb} \propto \sigma^2$ ), spanning  $\sim 5$  dex over the sample. Furthermore, it turns out that  $\sigma$ ,  $\Sigma$ , and  $P_{turb}$  tend to be systematically larger in the central kpc of barred galaxies and in more massive galaxies, indicating an influence of the local environment on the dynamical state of the molecular gas in the low-density regime.

To study the interplay between the local environment and the properties of GMCs, it is important to systematize the criteria used to define different environments or substructures of galaxies. This has been done in Querejeta, 2021 [49], using Spitzer (infrared) images to define environments on a PHANGS sample of 74 galaxies. The results show that molecular gas and SF are fairly evenly distributed in centers, bars, spiral arms, interarms, and disks. This result highlights the importance of the nucleus, since despite its small size, it hosts a comparable amount of SF to larger regions. In terms of density, galaxy cores in this study have the highest  $\Sigma_{mol}$  and  $\Sigma_{SFR}$ , while disks and interarm regions have the lowest. This result was also confirmed in Sun, 2020 [60], providing important empirical constraints on the physical connection between molecular cloud populations and their galactic environment. Further studies on the relationship between GMCs and their environment were performed by Kim, 2022[32], where they showed a quantitative link between galactic-scale environmental properties and small-scale GMC evolution.

High-resolution observations of PHANGS-ALMA allowed the study of SF laws on a sample of 80 galaxies, as done in Sun, 2023 [61]. By comparing the slope and scattering resulting from these laws with the tracer choices of SFR and CO-to-H<sub>2</sub> conversion factor, constraints on these values can be obtained. They also found that the properties of the molecular gas at cloud-scale resolution correlate with the properties of the host galaxy. Galaxies with higher stellar mass and more active star formation tend to host molecular gas with higher surface density and higher velocity dispersion. Again taking advantage of high-resolution observations, Pan 2022 [47] studied the gas-star formation cycle in nearby galaxies. They found that at 150 pc resolution, the distribution of star-forming regions depends on the stellar mass and Hubble type of the galaxy. High-mass, earlier-type galaxies have significant molecular gas reservoirs without H $\alpha$ -traced star formation, while lower-mass galaxies have substantial H II regions. Galactic structure adds complexity to the CO and H $\alpha$  emission distribution. Meaningful trends between galaxy properties and gas distribution are visible on a spatial scale of  $< 500$  pc, emphasizing the critical resolution for distinguishing star formation stages. Other work on the interplay between H II regions and molecular gas has been done by Zakardjian, 2023 [66]. in the context of studying the final stages of GMCs. They found that at the  $\sim 100$  pc scales accessible by the PHANGS-ALMA and PHANGS-MUSE data, pre-supernova feedback mechanisms in H II regions have a subtle but measurable effect on the properties of the surrounding molecular gas.

Most of the observations in the PHANGS project are of the CO(2-0) emission line, which requires the assumption of an  $R_{21}$  value to calculate the molecular mass.  $R_{21}$  is defined as the ratio of the intensity of the CO(2-1)/CO(1-0) lines, and is used to estimate the optical thickness of the molecular gas, from which the mass can be inferred. The use of high resolution observations in CO(1-0) with ALMA allows local variations in the  $R_{21}$  index to be taken into account, avoiding the need to assume a fixed value for all regions. Such observations have been made in NGC 2903 and NGC 3627 [9], and it has been found that  $R_{21}$  varies across the galaxy, consistent with changes in the temperature and density of the molecular gas. In particular, towards the center.

bibliografia.bib

## Chapter 2

# ALMA and basics of interferometry

The Atacama Large Millimeter/Submillimeter Array (ALMA) is an aperture synthesis interferometer located on the Chajnantor plain of the Chilean Andes (lat. $=-23.02917^\circ$ , long. $=-67.754649^\circ$ ) at an elevation of 5000 m above the sea level. These location offers the exceptionally dry and clear sky conditions required to observe over a broad range of frequencies in the millimeter and submillimeter range of the electromagnetic spectrum (since mm/sub-mm wave absorption is such a strong function of the amount of water vapour in the air).

The array is composed by 66 high-precision antennas arranged in a series of different configurations. Fifty of these antennas are 12-meter antennas (the 12-m Array), they are used to do interferometry and allow to have sensitive, high-resolution imaging. These fifty antennas are complemented by the Atacama Compact Array (ACA), composed of twelve closely spaced 7-m antennas (also known as the 7-m Array), and four 12-m antennas for single-dish (or Total Power) observations (the TP Array), to reduce flux losses of extended structures.

### 2.1 Interferometry: principles and concepts

Interferometry is the technique used to obtain very high angular resolution observations of astronomical phenomena. It's both used in the radio and visual regime based on the principle of interference of incoming electromagnetic waves. It involves coherent arrangement of sky signals received by two or more physically separated antennas pointing to the same object. The signals are interfered, allowing a sky brightness distribution to be sampled on an angular scale smaller than possible with a single antenna.

#### 2.1.1 Single dish response

The signal detection in millimeter/radio astronomy is based on the principles of the Fraunhofer diffraction theory: since the electromagnetic (EM) source is very distant, we can make the approximation of point-like source at infinity. Under these approximation the incident light is a plane and parallel waves front and its electric field distribution at the aperture of an antenna forms a diffraction pattern on the focal plane. The **power pattern**, or **beam**, of an antenna is the response in the focal plane to an EM signal, and is related to the power distribution through a Fourier transform of the diffraction pattern in the aperture.

The power pattern has a Gaussian-like primary maximum, called the main lobe or *primary beam* and several subsidiary maxima, called side lobes (Fig.2.1). The points which the *primary beam* falls to half its central value are called the Half Power points and the angular distance between these

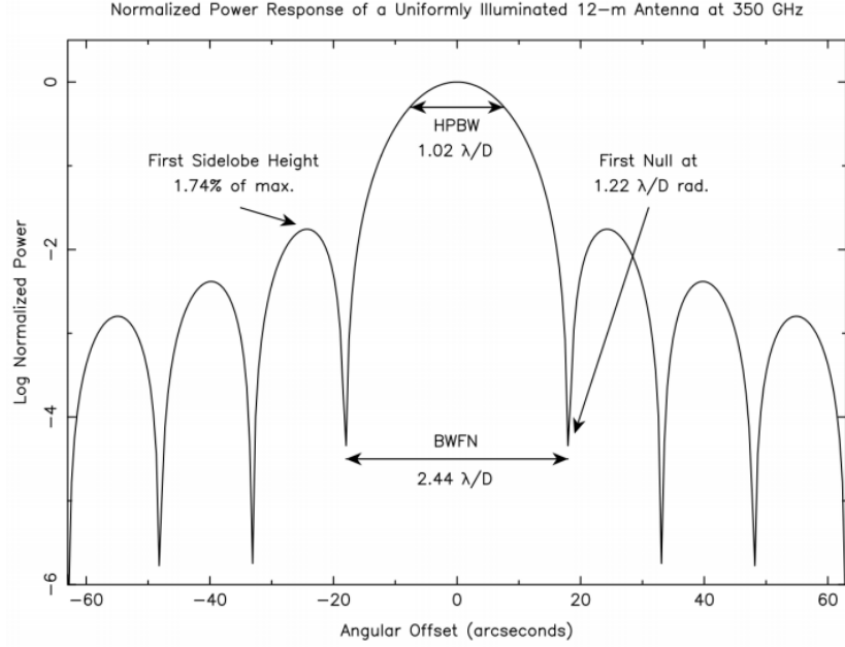


Figure 2.1: Normalized 1-D antenna power pattern for an uniformly illuminated antenna. The power is in log units. The HPBW of the main lobe is  $\sim 1.02\lambda/D$  and the FWBN is  $\sim 2.44\lambda/D$ . The angle of the first null, i.e. the resolution is  $\sim 1.22\lambda/D$

points is called the Half Power Beam Width (HPBW), and is given by

$$HPBW = 1.02 \times \frac{\lambda}{D} \quad [\text{rad}]$$

For radio astronomical applications one generally wants the HPBW to be small (so that the nearby sources are not confused with one another), and the side lobes to be low (to minimize the pickup of stray radiation).

The minima of the power pattern are called nulls. The angular distance between the first nulls is termed Full Width Between Nulls (FWBN) of the primary beam. It's given by

$$FWBN = 2.44 \times \frac{\lambda}{D} \quad [\text{rad}]$$

Half the FWBN of the primary beam,  $1.22 \times \frac{\lambda}{D}$ , is the Rayleigh resolution of the antenna<sup>1</sup>, i.e. the minimum angular distance between two objects for which they can be seen as separated.

The power response of an actual antenna, however, can be altered by various effects, such as surface imperfections or diffraction from other antenna components. The actual ALMA components were designed to provide an antenna power response with a nearly Gaussian primary beam and low side lobes, preserving as much resolution and sensitive as possible. The ALMA antennas have measured HPBW primary beam  $\sim 1.13 \frac{\lambda}{D}$ . This value is the so-called *field of view* (FoV) of a single ALMA antenna:

$$FoV \approx 1.13 \times \frac{\lambda}{D} \quad [\text{rad}]$$

<sup>1</sup>this is the Rayleigh's criterion which states that the angular resolution of a telescope is refraction limited and given by  $\theta \sim \frac{\lambda}{D}$

The total received power of each antenna is given by

$$P_{rec} = \frac{1}{2} \int_{4\pi} I_\nu(\theta, \phi) P_N(\theta, \phi) d\Omega$$

where  $\theta$  and  $\phi$  are the sky coordinates,  $I_\nu(\theta, \phi)$  the directional function of the sky brightness distribution and  $P_N(\theta, \phi)$  the normalized antenna power pattern (also known as the *Airy function*).  $A_e$  is the *effective area* (it depends of the direction of the incident wave, because the antenna works better in some direction than in others). The value  $\frac{1}{2}$  is due to the fact that the receiver is generally sensitive to only one mode of polarization. ALMA receivers, however, have been designed with two separate receptors, allowing both polarization modes to be detected at the same time, thus making the coefficient for ALMA equal to 1.

### 2.1.2 Aperture Synthesis

As we have illustrated before, the resolution of a single-dish observation increases with wavelength ( $\lambda$ ) and decreases with the diameter ( $D$ ) of the antenna. In particular, radio/sub-mm observations have typically poor resolution, compared with optical observations, because the value of  $\lambda$  is larger by several orders of magnitude. To achieve better angular resolutions, one has to either increase the diameter of the telescope further (which is not practical) or decrease the observing wavelength (which is not possible if we want to make radio observations).

To solve the problem, radioastronomers use the signals from two or more physically separated antennas and combine the signals through interferometry. With this technique, called *aperture synthesis*, it is possible to achieve a resolution of a radio telescope with a larger diameter, equivalent to the maximum distance between two antennas.

The distance between antennas in each pair is called *baseline* ( $b$ ). The power response of the antennas of a pair is time-averaged and cross-correlated. For a N antenna array one needs to measure  $N(N - 1)/2$  correlations simultaneously, this is done by a digital machine called the "correlator". The resulting power pattern will be the sum of such products of voltage patterns from element pairs.

Figure 2.2 shows a 2-elements interferometer. The antennas in the figure observe the same source but the signal is received at different times by the two elements: the signal arriving at antenna 1 experiences a geometrical delay given by  $\tau_g = bs_0/c$ , where  $s_0$  is the position observed by the antennas and  $c$  is the light-speed; it is therefore necessary to take this delay into account by applying an artificial delay to the signal path of antenna 2, so that the signals from both antennas arrive at the correlator with the same phase. The correlator multiplies and time-averages the signals coming from the two receivers and measures a quantity called *complex visibility*,  $\mathcal{V}$ . We can represent the visibilities in the *uv-plane*, which is the plane where visibilities live (Fig. 2.3). The  $(u, v)$  are the specific *spatial frequency* components of power pattern in the E-W and N-S directions respectively, these represent the lengths of the baselines projected onto a plane perpendicular to the direction of the source, measured in wavelengths at the time of the observation;  $(x, y)$  are the spatial components (in radians) of the source plane (i.e. the position in the sky plane).  $\mathcal{V}$  is a complex number and can be described by an amplitude  $A$  and a phase  $\phi$ , containing information about the source brightness and its location relative to the phase center, respectively. It can be proven that  $(u, v)$  is the Fourier transform of the sky brightness distribution  $B(x, y)$ , by the *van Cittert-Zernike theorem*:

$$\mathcal{V}(u, v) = \iint B(x, y) e^{2\pi i(ux+vy)} dx dy = A e^{i\phi} \quad (2.1)$$

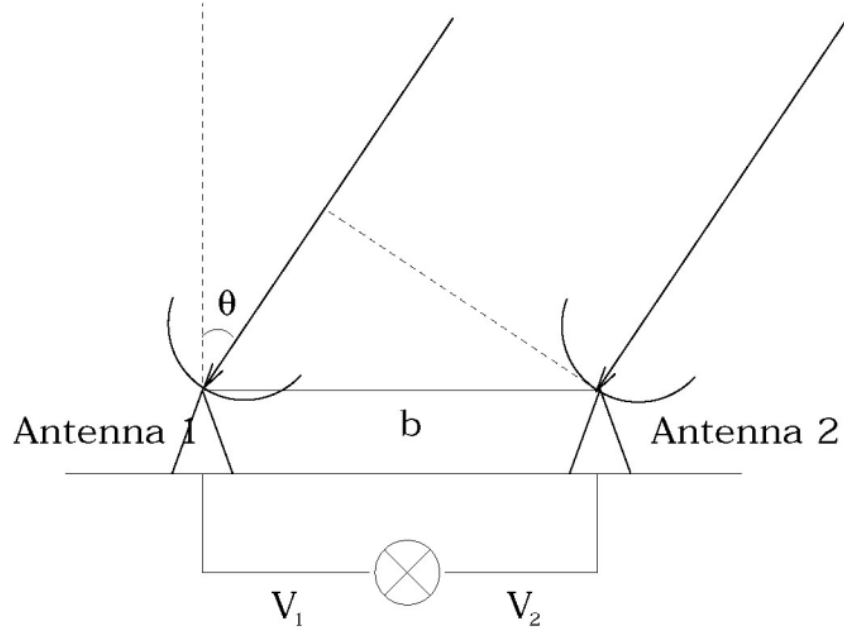


Figure 2.2: Two-element interferometer. There is a separation  $b$  (baseline) between the two antennas, and they are matched by a correlator. The system observes a portion of the sky  $s_0$ , at a distance  $\theta$  from the zenith. The signal arrives at antenna 1 with a geometric delay given by  $\tau_g = bs_0/c$ .

From Eq. 2.1 follows that the sky brightness distribution is in turn the inverse Fourier transform of the complex visibility distribution in the visibility plane:

$$B(x, y) = \int \int \mathcal{V}(u, v) e^{-2\pi i(ux+vy)} du dv \quad (2.2)$$

By measuring the complex visibilities distribution (in the  $uv$ -plane) we can determine the sky brightness distribution: each visibility has an amplitude and phase representing the brightness and relative position of emission on a specific angular scale. The image and its Fourier transform are conjugates of each other: from the inverse relationship of Fourier conjugate variables it follows that short baselines are sensitive to large angular structures in the source and that long baselines are sensitive to fine-scale structures. Indeed, each pair of antennas sample the sky brightness distribution on a scale inversely proportional to the projection of their distance on the sky. The response of the interferometer is sinusoidal (usually called *fringe*) and in the 1-D case, it samples spacing on the sky given by  $\lambda/b$ ; the antennas can sample the sky brightness distribution only on the scale defined by the wavelength of the sinusoid. Moreover, we note that fringe spacing also depends on the wavelength of emission, so observing shorter or longer wavelengths can sample smaller or larger angular scales, respectively.

A pair of antennas will only instantaneously sample one scale of the sky brightness distribution. Given the E-W and N-S separations of the pair, a visibility in the  $uv$ -plane is measured. The visibilities are complex functions with Hermitian symmetry so that a single sampling gives two points in the  $uv$ -plane,  $(u, v)$  and its complex conjugate  $(-u, -v)$ . In order to obtain the true sky brightness distribution it is necessary to sample the  $uv$ -plane as much as possible (ideally, to have a perfect image, the  $uv$ -plane should be evenly coated). This can be done by incorporating multiple

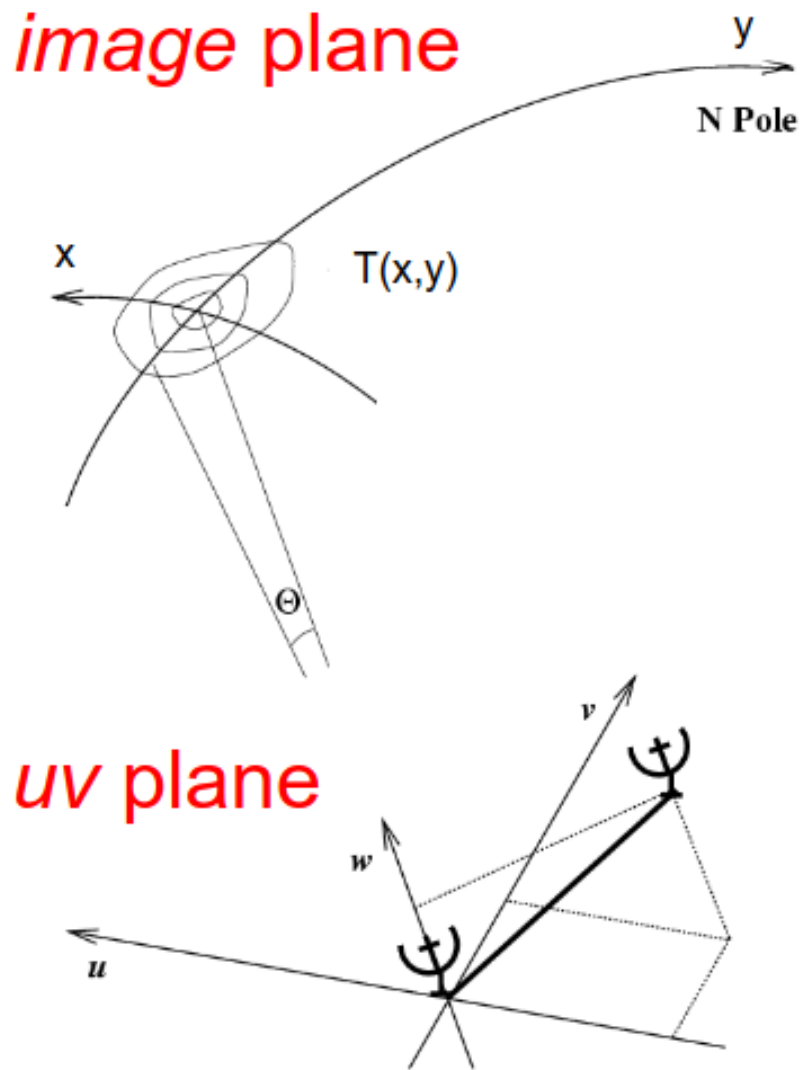


Figure 2.3: Schematic of the UV plane: A plane orthogonal to the line of sight containing the visibilities obtained from each pair of antennas (i.e., from each baseline). [45]

antennas into an array and by arranging the antennas in different configurations. Furthermore, we can observe the target repeatedly as it moves across the sky by the Earth’s rotation effect, which changes the projected separation between the antennas, allowing us to sample more angular scales.

### 2.1.3 Interferometer properties

#### Field-of-view

As noted before, each antenna of the array has its own power response on the sky, the primary beam, given by its Airy function  $P_n = \mathcal{A}(l, m)$ ; it means that the individual antenna response limits the extent of an interferometric image made with a single pointing. In practice, the HPBW of the primary beam serves as the “field-of-view” of the single-pointing interferometric image, so it depends on  $\lambda/D$ . If a map size larger than the full width at half maximum (FWHM) of the primary beam is required, multiple pointings in a mosaic pattern must be observed to capture the sky emission. This provides an increase in the areal coverage but requires more observing time. The sensitivity of the mosaic will depend on the spacing between the individual pointings.

#### Angular resolution

The resolution of an image is defined as the compactness of the central feature of the beam, i.e. half its FWHM. In the case of interferometric observations the beam is usually called *synthesized beam* and the resolution is typically approximated to first order by the FWHM of a Gaussian fit to the central feature of the beam. The arrangement of interferometer antennas affects the resolution: in a compact configuration the central beam feature is wide, resulting in low resolution, while an extended configuration gives higher resolution since the central beam feature is narrow. So the scale discernible in the image is limited by these maximum baselines.

At first approximation, the angular resolution provided by an interferometer is given by:

$$\theta_{res} = k\lambda/B_{max} \quad [\text{rad}]$$

where  $k$  is a factor that depends on how the visibilities are weighted and  $B_{max}$  is the longest baseline of the array.

#### Maximum recoverable scale

Interferometric array observations have a significant limitation in that they are insensitive to large angular scales. This insensitivity occurs because the arrays cannot sample spatial frequencies lower than those sampled by a baseline equal to an antenna diameter (because we cannot physically “overlap” two antennas). As a result, visibilities at or near the origin of the *uv-plane* are not sampled, which is known as the *zero-spacing problem*. For this reason, an interferometer image has a *maximum recoverable scale*, and it can be computed by:

$$\theta_{mrs} \approx 0.6\lambda/B_{min} \quad [\text{rad}]$$

where  $B_{min}$  is the shortest baseline of the array.

#### Sensitivity

Sensitivity can be defined as the lowest flux detectable by our instrument, with anything below this limit being classified as noise. In this context, noise refers to the random fluctuations caused

by the variability of a data population, as determined by the root mean square (RMS), which can be estimated using the following formula:

$$\sigma_{RMS} = \frac{2k}{\eta} \frac{T_{sys}}{\sqrt{\Delta t \Delta \nu} \sqrt{N_{ANT}(N_{ANT} - 1)A_e}} \quad (2.3)$$

where  $k$  is Boltzmann constant,  $\eta$  is the instrumental efficiency ( $\sim 0.9$ ),  $\Delta T$  is the total time on-source,  $\Delta \nu$  is the bandwidth,  $N_{ANT}$  the number of antennas and  $A_e$  the effective area of each antenna.  $T_{sys}$  is the system temperature (see 2.2.1), which takes into account the effects of the atmosphere on the interferometer.

Located at an altitude of 5000m in the world's driest place, ALMA benefits from an extremely low  $T_{sys}$  value. This, combined with a large number of antennas, enables exceptional sensitivity (therefore a small  $\sigma_{rms}$  value) even during brief observations.

## 2.2 Calibration

The data received from the sources is corrupted by atmospheric and instrumental effects. As a result, calibration is necessary to remove these defects before proceeding with analysis. Hamaker-Bregman-Sault *measurement equation* describes the relation between the observed visibilities ( $V_{obs}^{ij}$ ) and the ideal visibilities ( $V_{real}^{ij}$ ), for a baseline between antenna  $i$  and  $j$

$$V_{obs}^{ij} = G^{ij} V_{real}^{ij} \quad (2.4)$$

where  $G^{ij}$  is a matrix that contains the gain factors that represent the combination of all the corruption factors related to the baseline  $ij$ .

To perform calibration, we make two assumptions. The first assumption is that all data corruptions are associated only with individual antennas and not with their combination, so we can factor our equation antenna-by-antenna:

$$V_{obs}^{ij} = G^i G^j V_{real}^{ij} \quad (2.5)$$

The second assumption is that the frequency and time dependencies are independent of each other, thus we can further decompose the Gain matrix into a frequency dependent part and a time dependent part:

$$G^i(\nu, t) = B^i(\nu) J^i(t) \quad (2.6)$$

This assumption is reasonable because the frequency error is primarily caused by the antenna electronics and remains constant over the observing time, whereas the atmosphere primarily introduces time dependent effects. Here  $J^i(t)$  is the component dependent on the atmospheric condition and the  $B^i(\nu)$  is the one dependent on the instrumentation and its efficiency.

To calculate the correction factors, we observe calibrator sources and solve the measurement equation for them. The antenna-based gain factors are then determined and stored in calibration tables, which are applied to the data to correct the observed visibilities.

### 2.2.1 $T_{sys}$ and WVR

At millimeter wavelengths, two additional important calibration are needed, because the astronomical signals are significantly degraded by the Earth's troposphere. The two main effects are:

1. **Absorption of the signal:** the atmosphere acts as a black body emitter, leading to an attenuation of the signal in some spectral ranges. To correct for this effect, an Amplitude Calibration Device (ACD) is installed in each ALMA antenna. The ACD allows to measure the variation in frequency of the System temperature ( $T_{sys}$ ). The  $T_{sys}$  is the temperature equivalent to the total noise power received by a telescope, and it's given by:

$$T_{sys} \approx \frac{T_{rx} + T_A(\text{sky})}{\eta_{eff} \times \exp[-\tau_0 \sec z]} \quad (2.7)$$

Where  $T_{rx}$  is the electronic noise and  $T_A$  is the antenna temperature of the sky which includes contributions from the atmosphere, antenna response and cosmic microwave background (CMB).  $\eta_{eff}$  is the antenna efficiency, related to the antenna gain and its power pattern. The  $\exp[-\tau_0 \sec z]$  factor represents the transmission of the atmosphere, where  $\tau_0$  is equal to the zenith atmospheric opacity and  $\sec z$  is zenith secant which gives an estimate of the airmass at transit.

2. **Delay of the signal:** this effect is related to the amount of precipitable water vapor (PWV, given in mm) on the atmosphere and its variation in the sky above the interferometer, that causes atmospheric turbulence. This turbulence leads to a phase variation, that results in a de-correlation of the astronomical signal.

In order to correct for these phase fluctuations, ALMA has placed a Water Vapor Radiometer (WVR) on each 12-m antenna which samples the water line at 183 GHz to give an estimate of the PWV quantity on the atmosphere during the observation. To ensure the effectiveness of WVRs, measurements must be taken at a cadence that is rapid enough to accurately map the fluctuations in the atmosphere. For that reason ALMA WVRs register the atmospheric effect with a cadence of one second.

These calibrations are performed without observe specific calibration sources. The corrections given by the specific devices are applied to the data prior to proceeding to the calibration via known sources observations (calibration sources).

### 2.2.2 Bandpass calibration

It is necessary to calibrate the frequency response of each antenna, that leads to determine the  $B(\nu)$  in equation 2.6. To perform this calibration, we rely on the observation of a bright source with a flat spectrum. It can be located in any part of the sky. Typically, a quasar is observed for a sufficient duration to achieve a high signal-to-noise ratio. In an ideal scenario where corruptions are absent, a perfect interferometer would exhibit a uniform response across all frequencies, with a phase of 0, if the source is at the center of the pointing (phase center). It is evident that these conditions cannot be met in real-world, hence it becomes necessary to correct the effects caused by both instrumentation and external factors through a process known as *bandpass calibration*.

To determine the bandpass correction, an observation of the calibrator is conducted and any significant phase variation over the bandpass observation is eliminated, and the amplitude and phase corrections are computed as a function of frequency and stored in a table. The bandpass response is highly stable and almost time-independent, which ensures that the bandpass determination remains consistent throughout each observing block (which lasts for about an hour). This solution can be applied to all the observed data in a single run.

### 2.2.3 Time dependent calibration

In addition to calibrating the frequency response, it is essential to calibrate the data, in amplitude and phase, as a function of time. In this way we find the  $J(t)$  in eq. 2.6. To achieve this, it is required to observe a known pointlike source in close proximity to the target. This ensures that the signal passes through the same layer of air. The observation needs to be repeated before and after the target to determine the corrections which are linearly interpolated when applied to the data. To calibrate the phase response, it is necessary to define a reference antenna whose phase will be arbitrary fixed at 0 (typically the antenna located at the center of the array is chosen).

### 2.2.4 Flux calibration

It is necessary to assign a physical scale to our visibilities, which means converting the amplitudes of our visibilities into Jy. This is achieved by using a known source with a known flux to rescale our observations.

## 2.3 Imaging

After calibrating the data, the source's image is reconstructed. The brightness distribution of the source corresponds to the Fourier transform of the complex (and ideal) visibility function (see Eq. 2.2). However, the interferometer only partially samples this visibility function. It's important to note that each baseline generates only one point in the **uv-plane** (two if we include the complex conjugate). Although using a larger number of antennas and taking advantage of the Earth's rotation to acquire more points has resulted in significant improvement, the uv-coverage still remains limited. As a result, a discrete *sampling function*  $S$  must be defined, which takes a value of 1 at the points where visibility has been acquired and 0 elsewhere. In this way, the true visibilities distribution ( $V^{true}$ ), which corresponds to an ideal total coverage of the *uv-plane*, is 'filtered' by the sampling function obtaining the observed calibrated visibilities  $V^{obs}$ :

$$V^{obs}(u, v) = S(u, v) \cdot V^{true}(u, v) \quad (2.8)$$

The inverse Fourier transform of eq. 2.8 represents the observed brightness distribution  $I^{obs}$ , which is called **dirty image**. A product in the real plane becomes a *convolution* in the Fourier's plane, so the dirty image is the convolution between the inverse Fourier transforms of the sampling function and the true visibilities, respectively:

$$I^{obs} = \mathcal{F}^{-1}(V^{obs}(u, v)) = \mathcal{F}^{-1}(S(u, v)) \otimes \mathcal{F}^{-1}(V^{true}(u, v)) \quad (2.9)$$

The inverse Fourier transform of the sampling function is called **dirty beam** and represents the *point spread function* (PSF), i.e. the way in which the system would see a point source. An ideal PSF has a Gaussian shape. Nonetheless, the incomplete coverage of the UV plane results in a non-perfect Gaussian shape of the PSF (which will have some side lobes) leading to artifacts in the image.

From the eq. 2.9 we can see that in order to obtain the real image of the source, the dirty image must be deconvolved from the dirty beam, a process known as cleaning. The CLEAN algorithm is utilized for this purpose, which involves iteratively removing the brightest pixels and the corresponding sidelobes introduced by the dirty beam from the dirty image and transferring these peaks to a model image while recording their coordinates and flux. This process continues until a threshold flux is reached, this threshold is set to a value that is an integer multiple of the root mean

square ( $\sigma_{RMS}$ ). The end result is a uniformly noisy residual map (i.e. the dirty image without peaks). The peaks are multiplied by the **clean beam** (the elliptical Gaussian fitting of the central lobe of the dirty beam) and then added back to the residual (restoring).

### 2.3.1 Visibility Weighing

To work, the software used for the imaging divides the UV plane into a uniform grid. However, because the array has more short baselines than long baselines, the former are sampled more frequently than the latter. This can result in a significant reduction in angular resolution. There are different ways to weight the visibilities, the main ones are:

1. **Natural:** Retains the "default" weighting just described, in which visibilities are weighted only by the data weights ( $\omega_i$ ) calculated during filling and calibration, which should be equal to the inverse noise variance on that visibility ( $\sigma^2$ ). With this setup, the image weight of a sampled visibility  $i$  will be:

$$w_i = \omega_i = \frac{1}{\sigma^2} \quad (2.10)$$

2. **Uniform:** In this case, each scale is given equal weight. The data weights are initially computed according to the "natural" weighting scheme. The data is then mapped to multiple cells in the UV plane. When multiple visibilities occupy a single UV cell, their weight is reduced in proportion to the number of visibilities in that cell. This allows the weight of the long baselines to be "balanced" with the weight of the short baselines. While this weighting mode provides the highest resolution in the image, it does not optimize system noise.

Another way to weigh visibilities is to choose the *Briggs* method of weighing, which represents a middle ground between uniform and natural weighting. A sub-parameter known as *robust* is employed to choose the preferred balance between uniform and natural weighting levels. Robust takes value between -2.0 (close to uniform weighting) to 2.0 (close to natural).

## Chapter 3

# Scientific target and observational data

The primary objective of this study is to observe and comprehend the properties of Giant Molecular Clouds (GMCs) within various environments in the galaxy NGC 3627. To achieve this, we utilize observations taken with ALMA during its third observation cycle in the Band 3, to observe the CO(1-0) emission line (rest frequency 115.27 GHz), allowing us to determine the mass of molecular gas within these clouds.

We calibrated and imaged the available data using the CASA software, obtaining the line and continuum image of the galaxy in question. To analyze the emission, we extracted from the velocity cube the moments of order 0, order 1 and order 2, providing the integrated intensity, the velocity and velocity dispersion, respectively.

### 3.1 NGC 3627

NGC 3627 is a star-forming galaxy classified as low-ionization nuclear emission-line region (LINER/Type 2 Seyfert galaxy) [26]. It has a prominent bar structure with two strong spiral arms emanating from the bar ends and associated with massive star formation [6], both of which (arms and bar ends) are very appealing features for the study of GMCs and SFR in different environments. Figure 3.1 shows the latest image of this galaxy taken by the James Webb Space Telescope. NGC 3627 is located at a distance of about 11 Mpc. At this distance, 1 arcsec corresponds to about 50 pc, allowing to properly study GMCs having sizes of the order of about 10-100 pc (see section 1.5). NGC 3627 is located at a distance of about 11 Mpc. This is a relatively close and favorable distance, since at this distance 1 arcsec corresponds to about fifty parsecs. This maximizes the angular resolution.

In addition, the object has an almost entirely face-on orientation (inclination angle of 65 deg with respect to a position angle  $\theta_{PA} = 170^\circ$  [11]) which enables us to easily observe the substructures of the galaxy in their fullness (the whole bar, both bar ends, arm and inter-arm regions included).

Observations of the centre, a bar-end and a spiral arm in the 3-mm band, using the IRAM 30m and Nobeyama 45-m telescopes, revealed the detection of  $\sim 10$  molecular species in each of these regions. Notably, the chemical composition was found to be similar among these regions[62]. When mapping NGC 3627 in HCN and HCO+, evidence of recent star formation was uncovered in the central region as well as at the bar-ends[44]. In fact, NGC 3627 exhibits strong burst signatures at the two bar ends (north and south) resembling structures found in W43 mini-starburst within our Milky Way[6] (see section 1.5.1). Understanding whether the phenomenon we see in our MW is common to other galaxies can help shed light on the physical phenomena behind SF and how they

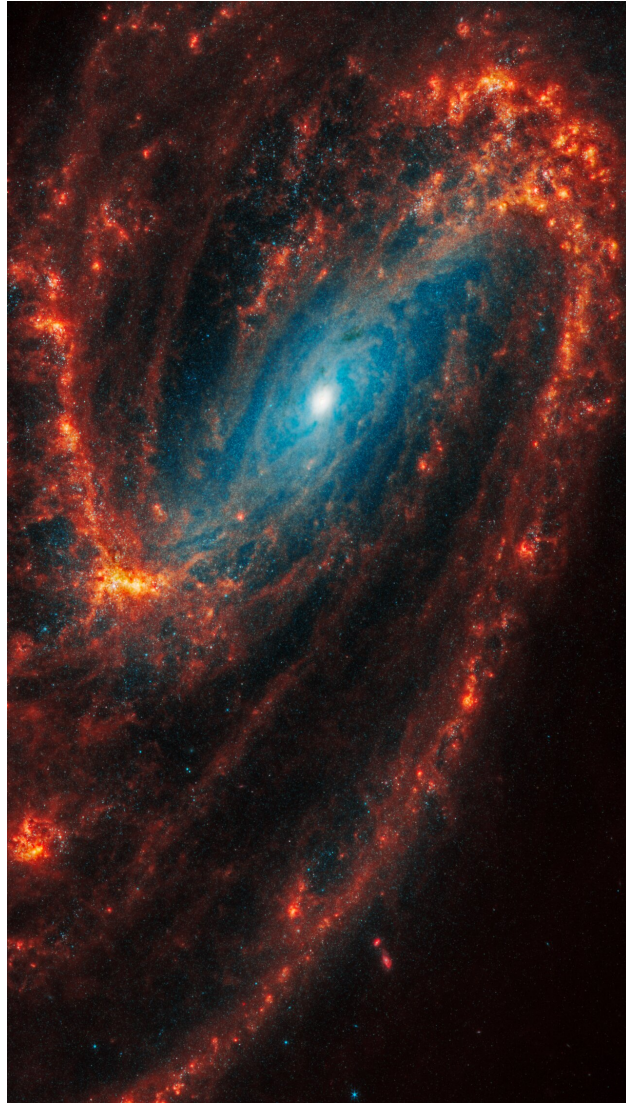


Figure 3.1: Webb’s image of NGC 3627 shows a face-on barred spiral galaxy anchored by its central region, which has a bright blue central dot. It is surrounded by a bar structure filled with a lighter blue haze of stars, which forms a large, angled oval toward the top. Two large distinct spiral arms appear as arcs that start at the central bar. One starts at left and stretches to the top and another starts at right and extends to the bottom[22]. Credit: NASA, ESA, CSA, STScI, J. Lee (STScI), T. Williams (Oxford), PHANGS Team. ESA/Webb

Dataset	Acquisition date (dd/mm/yyyy)	$N_{ant}$	Observation time (s)	$B_{max}(m)$
X10a8	24/01/2016	47	4095	1170
X1db0	16/03/2016	39	4082	810
X5eee	11/08/2016	38	3955	780

Table 3.1: Details about our datasets.  $N_{ant}$  denotes the number of antennas while that  $B_{max}$  denotes the maximum baseline.

SPW	Central Freq. (GHz)	Number of channels
23	102.5	128
25	115.3	3840
27	112.8	960
29	100.8	1920

Table 3.2: Description of used spw.

are affected by the environment.

Finally, as this galaxy hosts an Active Galactic Nucleus (AGN), the study of NGC 3627 can provide insights into the extent to which AGN activity influences star formation in the nucleus and throughout the entire galaxy.

## 3.2 ALMA Observations

NGC3627 has been observed in 2016 with ALMA 12m array during the ALMA Observation Cycle 3. During this observation cycle, ALMA had 48 antennas available (it now has 53).

Multiple observations have been taken, with different configurations, giving us 3 different datasets with different maximum baselines. Having multiple datasets is an advantage for our work, since greater coverage of the UV plane (both for different antenna configurations, as well as for different relative positions of the source at the time of observation) mean a more accurate image of the source under investigation. Table 3.1 reports the details of the observations and Fig. 3.2 shows the antenna configuration for X1db0 dataset.

Since the purpose of our work is to observe the emission of CO(1-0), which - at the redshift we are at ( $z=0.00241$ ) - is observed at 114.992 GHz, our data are taken with to ALMA Band 3. This band covers a spectral range from 84 GHz up to 116 GHz[15]. The observation are taken in four spectral windows (spw): 23, 25, 27, 29; the details of which are given in Table 3.2. The CO(1-0) line is observed in spw 25. We use the other spw to determine the continuum.

The available data allows us to achieve an *ideal* resolution of 0.47 arcseconds, which corresponds to a linear resolution of approximately 25 parsecs. However, by combining the different data sets, the effective resolution will be lower. The FoV of our observations is about 2 kpc and results in a MRS of approximately 2.5 kpc. Given that the diameter of NGC 3627 is approximately 26 kpc (De Vaucouleurs 91), observing the entire galaxy necessitates multiple pointings to create a mosaic covering various observed regions. In fact, each of our datasets consists of 23 pointings, covering the entire galactic disk and most of the spiral arms, roughly as shown by the yellow rectangle in Figure 3.3.



### 3.3 ALMA Data reduction

We conducted a calibration process to correct for corruptions caused by the atmosphere, the instruments and phase shifts between the antennas, while also converting our visibility data into physical units of flux density (Jansky, Jy. Introduced in Chapter 2). Following the calibration, we proceeded with imaging and identifying both the continuum and the CO(1-0) emission line, for which we extracted the moment 0, 1 and 2; providing the integrated line intensity and the velocity distribution, respectively.

#### 3.3.1 CASA

CASA, which stands for Common Astronomy Software Applications, is the primary data processing software for single dish and interferometric data, especially developed for ALMA and the Karl G. Jansky Very Large Array (VLA). CASA consists of a collection of applications implemented in C++, accessible through an interactive Python interface. It allows the conversion of data from the radiotelescope into the so called MeasurementSet (MS), where the interferometric or single-dish data details are stored in tables and sub-tables using high-level tasks. These tasks perform specific, well-defined steps in data processing, such as plotting, flagging, calibration, or imaging. CASA also includes a range of applications with Graphical User Interfaces (GUIs) for inspecting visibility data, image products, and metadata. Among the most widely used GUIs in CASA are *plotms* for diagnostic plotting of visibility and calibration-table data and the 'CASA viewer' for visualizing image products.[5]

#### 3.3.2 Data import, inspection and flagging

First we need to download and import the data that ALMA has collected from the ALMA Science Archive<sup>1</sup>. The downloaded package is organized into various directories and subdirectories. It includes essential tables for calibration, Python scripts required for data reduction in CASA as well as the raw data. This data that we have imported, is stored in the ALMA Science Data Model (ASDM) format, which contains the meta-data (headers, description of the observation setup, etc) and the raw visibility. This import is done through CASA's 'importasdm' task, which converts from ASDM format to CASA's suitable format, i.e., MS format.

Therefore, 'a priori flagging' was performed, involving the removal of data that we know, a priori, are not used in the calibration. Some visibilities have been identified as non necessary (flagged), due to:

1. *Shadowing*: visibility collected by antennas which, due to a particular angle of inclination, were partly obscured by the shadow of nearby antennas.
2. *Pointing and atmosphere*: consist on the scans performed to check the pointing precision and for the atmosphere calibration. They are not needed.
3. *Auto-correlation*: They are the result of combining the signal from each antenna with itself. They are flagged due to their high noise levels.
4. *Edge channels*: Represent the data collected by the edge channels of each spw. Since they are very noisy (compared to the center channels), they are flagged.

---

<sup>1</sup><https://almascience.nrao.edu/aq/?observationsSourceName=ngc3627>

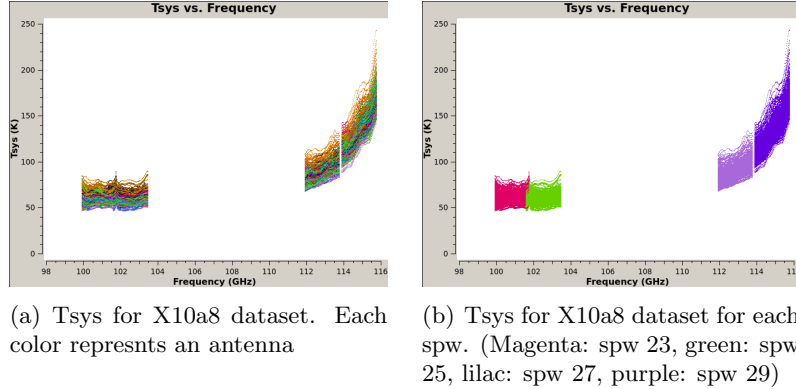


Figure 3.4: X10a8 Tsys

This "flagging" can be done directly from CASA, without any initial data inspection, using the task 'flagdata'. Another type of flagging we conducted is manual flagging, which involves visual data inspection. Using the CASA *plotms* GUI, we monitor the behavior of all available antennas. If any antennas deviate from the expected trends followed by the others, they are flagged as potentially faulty.

Using this procedure, for dataset X10a8 we flagged antenna DA50 in scans 13, 14, and 15 and antenna DA59 in scans 20, 21, and 22. For dataset X1db0, we flagged antenna DV04 because it had phase drift and antenna DA48 because it had low gain. For the X5eee dataset, we flagged antennas DA49, DA50, DA53, DA62, DA65, DV04, and DV08, all during scan 13.

### 3.3.3 A priori calibration

The initial corrections that need to be applied to our data are those that have to do with the corruption due to the atmosphere, both in terms of attenuation (due to the emission of the atmosphere) and phase shift (resulting from the turbulence due to the vapor of water). [see section 2.2.1]

**WVR correction:** From the data collected by the WVRs, and using the Python scripts useful for calibration (found in the previously downloaded package), we generated the WVR tables. We use these tables to apply this time-dependent correction to our data.

**$T_{sys}$  correction:** Likewise, the  $T_{sys}$  values, measured by de ACD, are stored in the .MS and we can compute them. Once these  $T_{sys}$  gains are computed, it is useful to visually inspect the trends in order to identify specific atmospheric features and potential unusual behaviors specific to individual antennas or spwm, as is done in Fig. 3.4, where the Tsys trend for the X10a8 dataset is shown: the trend appears to be almost the same for all antennas in the different spw. In this case, the visual check can be considered passed.

### 3.3.4 Bandpass calibration

The first correction matrix we get is the one related to the bandpass, containing amplitude and phase corrections as a function of frequency. As mentioned in section 2.2.2, this correction is performed by observing a calibrator, i.e. a known (bright) source whose (flat) spectrum we know.

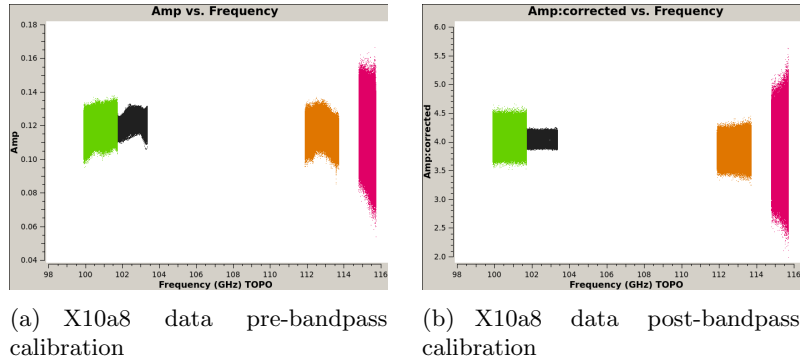


Figure 3.5: The trend of amplitudes as a function of frequency before (a) and after (b) bandpass calibration: the amplitude value is stabilized around a constant value. Different colors correspond to different spw.

The deviations between the model associated with the calibrator and what we observe are computed in the table of corrections to be applied.

For our three data sets, the source used as bandpass calibrator was J1058+0133. The CASA task that performs this task is 'Bandpass', which determines a normalized frequency correction in amplitude and phase for each antenna, scan and polarization. We chose DV06 as the reference antenna for the first data set, DV08 for the second and DV05 for the third.

Before proceeding with this calibration, it is necessary to set all (random) phases of the visibilities to zero. This is because otherwise the averaged amplitudes would give a value close to zero (the averaging is done over the entire scan time, i.e. the source observation time, which in the case of the bandpass calibrator is about 10 minutes; whereas the visibilities are acquired every about 6 seconds). To perform this "pre-correction", we use the *gaincal* task, which gives us a pre-bandpass table in which the phases are corrected as a function of time. These corrections are then applied "on the fly" in the 'bandpass' task to prevent the visibilities from combining destructively.

The result of bandpass calibration is to bring the amplitude and phase values to an almost constant value with respect to frequency (Fig. 3.5).

### 3.3.5 Amplitude and phase vs time calibration

In this step, we address calibration for time-dependent corruptions, employing the J1118+1234 point-like source as phase calibrator. To execute this correction, we utilize all three calibrators, calculating the gain matrix and applying the bandpass correction "on the fly". It's important to note that corrections are computed for all calibrators, and specifically, those determined for the phase calibrator are subsequently applied to the target. Prior to this calibration, the phases of each baseline are random, covering values from  $-180^\circ$  to  $180^\circ$  (Fig. 3.6 (a)). Then, because the calibrator is a point source observed at the center of the pointing, the phases are brought to zero, using the same reference antenna (Fig. 3.6 (b)).

In this step, we rescale the solutions obtained from the calibrators to their true flux in physical units (Jansky), using Callisto as a reference (flux calibrator) for the first two datasets and J1058+0133 for the third.

With this last procedure we obtain the time correction table which, together with the previously obtained bandpass correction, allows us to calibrate the observations of our target (NGC 3627).

The visibilities of NGC 3627 are taken in a time between two phase calibrator observations (Fig. 3.7), and the value of the target correction is assigned by a linear interpolation of two adjacent

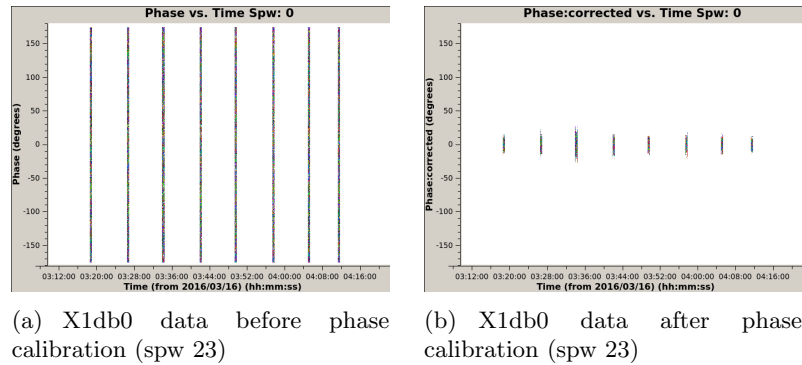


Figure 3.6: Phase trend before and after calibration, corresponding to data set X10a8 in spw 23. Before (a): the phases are random, for each baseline. After (b): The phases are brought to zero.

calibrator corrections. In other words, we assume that if there is a change in the atmosphere between two consecutive phase calibrator observations, that change will have a linear behavior.

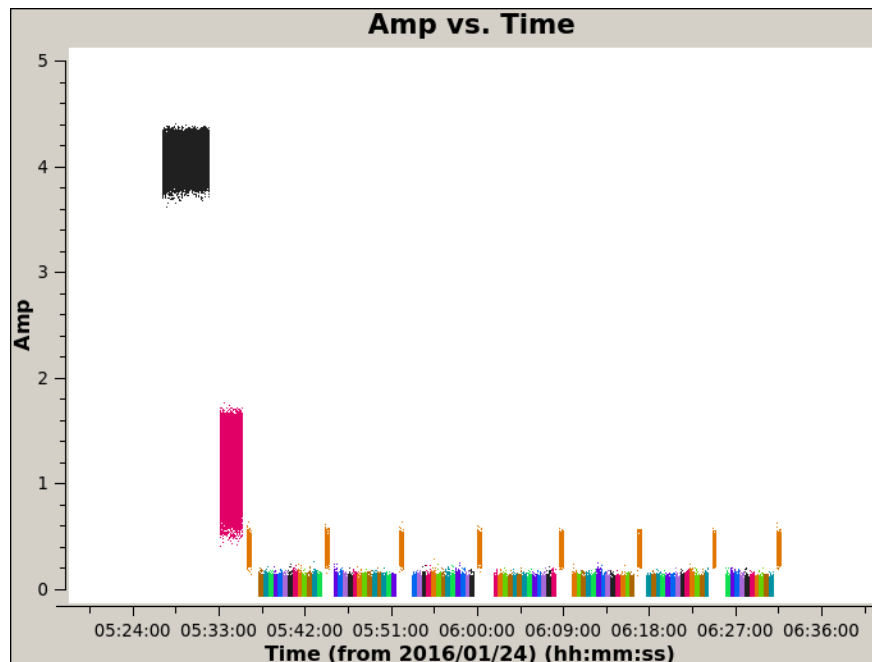


Figure 3.7: Amplitude vs. time plot for data set X10a8, already calibrated. The first two set of visibilities correspond to the bandpass and flux calibrators. The points in orange correspond to the phase calibrator observations interspersed with the science target observations.

### 3.3.6 Inspection of calibrated data

At this point, the calibration is complete. In Fig. 3.7 we can see the amplitudes of our source and calibrators already corrected for the various distortions listed above. We can now work on our source data. For example, in Fig. 3.8 we have a plot of the fluxes of NGC 3627 (of all the fields that make up the mosaic) as a function of frequency, averaged over time. What we observe is an emission line around 115 GHz corresponding to the CO(1-0) emission. The double hornet shape of

the line suggests gas rotation, with one velocity component approaching us and another receding.

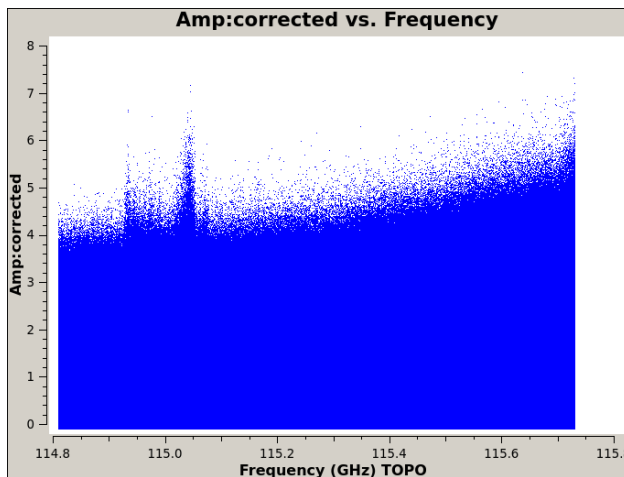


Figure 3.8: Emission of the source from X10a8 data, viewed through spw 25, as a function of frequency (GHz). We notice a line emission around 115 GHz: this is the CO(1-0) line. The observed double peak tells us that the gas is in rotation.

We can derive a similar plot, as shown in Fig. 3.9, where we still have fluxes, but as a function of velocity. The plot is colored by pointing, and we can see that the peaks are associated with specific regions in the galaxy. We can also see, from the broadening of the line, that the velocity range it covers is from 500 to 900 km/s. The channel width of the spw where the line appears is 244 kHz, which gives us a velocity resolution of about 0.6 km/s (Eq.3.1), which is too high to sample such a large line (of about 400 km/s).

$$\Delta v = \frac{\Delta \nu}{\nu} c \quad (3.1)$$

We lighten the information load by smoothing the data to a velocity resolution of 10 km/s, which is sufficient for a line of this width.

With our calibrated visibilities and having identified the channels in which the line is located, we can proceed with the image reconstruction of NGC 3627.

### 3.3.7 Imaging

As we mentioned in section 2.3, the imaging process can be summarized as the deconvolution of the dirty image from the dirty beam. We use the CLEAN algorithm to perform it, using CASA's *tclean* task.

We first performed the imaging of continuum and line emission for each of our data sets, and then - once the quality of the result is confirmed - merge them to treat them as a single data set, taking into account the fact that the X10a8 data set has a larger baseline than the other two data sets and therefore the corresponding resolution will be better.

#### TClean

To perform this task, we need to provide some parameters, such as *cell*, which refers to the size of each pixel, and *imsize*, which, as the name suggests, refers to the total size of the image (in pixels). To define the *cell* parameter, we must take into account Nyquist's sampling criterion, which tells

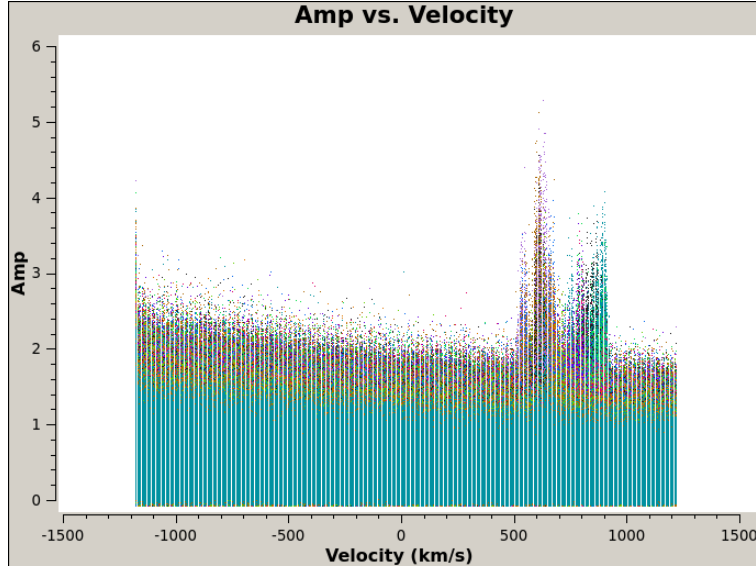


Figure 3.9: Source emission as a function of velocity, with different colors for different fields (target areas). Line emission CO(1-0) is noted.

us that to accurately represent a continuum signal by digital sampling, it must be sampled at least twice within the resolution element. In other words, the pixel size must be at most half the size of the beam. To make sure we meet this criterion, we set the pixel size to  $\theta/4$ , which in our case is 0.2 arcsec. Based on this, we can also set the value of the second parameter, choosing a number of pixels that will be able to contain the entire image. In our case we choose an *imsize* of 1150 pixels, covering a full area of 240 arcsec.

Another parameter that needs to be set is the weighting of the visibilities (see section 2.3.1). In our work, because of the little improvement that the use of uniform weighing represented, it was decided to keep the natural weighing.

In our work, because of the little improvement that the use of uniform weighing represented, it was decided to keep the natural weighing.

First, we apply the clean algorithm to get the continuum emission image. To do this, we exclude the channels where the line is present, i.e. we do not consider channels 200 to 1500 of *spw* 29 (we will stay wide so as not to run the risk of contaminating the continuum). This specification is made in the *spw* parameter of the *tclean* task.

The CLEAN work continues until we get a map that is uniformly noise, i.e. until we reach a threshold in flux, which in our case is given by  $2\sigma_{RMS}$ . To derive this RMS we used the ALMA sensitivity calculator. In our case, the expected rms value is  $2.5e-3$  Jy, so we will use  $5e-3$  Jy as the threshold value.

In addition to the continuum image (Fig. 3.10), we also extract the emission line image. For this we use the task *uvcontsub*. This task performs continuum fitting and subtraction in the UV domain. It does this by estimating the continuum emission through a polynomial fit of the line free part of the observed *spw*. We define the spectral windows and channels for the fit using the *fitspw* parameter and select a fit order of 1. The resulting fit serves as a continuum model across all channels. This fitted continuum spectrum is then subtracted from the specified spectral windows (*spw*), resulting in an output MeasurementSet (.ms file) containing only the intended line emission.

With the continuum subtracted, we restart the *tclean* task, but this time with additional parameters, including a rest frequency of our line emission (114.99 GHz, which is the frequency at

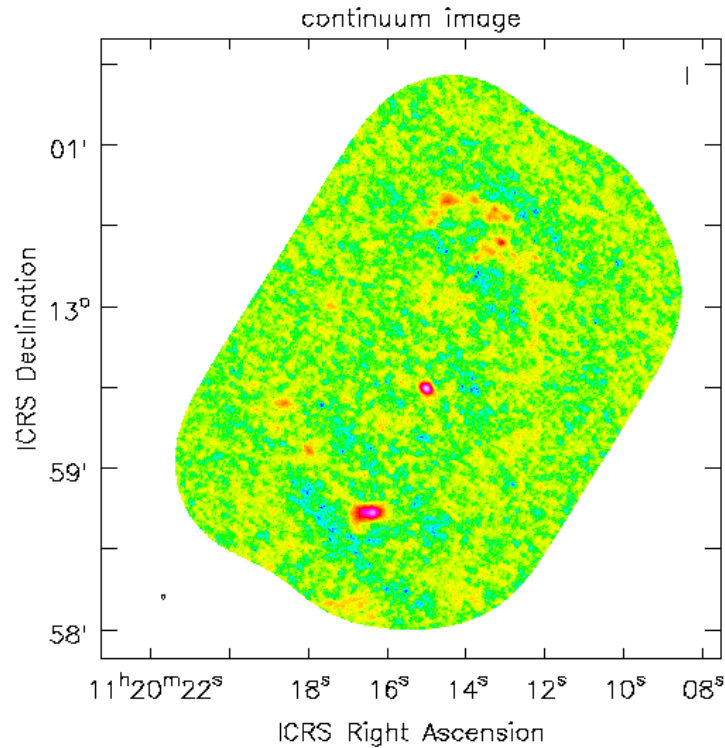


Figure 3.10: Image of the continuum emission of NGC 3627. The synthesized beam is shown in the lower left corner, with FWHM size of  $1.667'' \times 1.511''$  and position angle of  $50.154^\circ$ .

which we observe this emission, at the redshift of the target) and we set the parameter *specmode=cube*, this is to obtain a data cube that gives us the channel-by-channel emission in velocity, i.e. with a cadence of 10 km/s (which is the width in velocity of the channels). We specify this cadence in the *width* parameter.

In Figure 3.11 we can see some frames of the resulting velocity cube.

Table 3.3 shows the main characteristics of the continuum image and the velocity cube. RMS

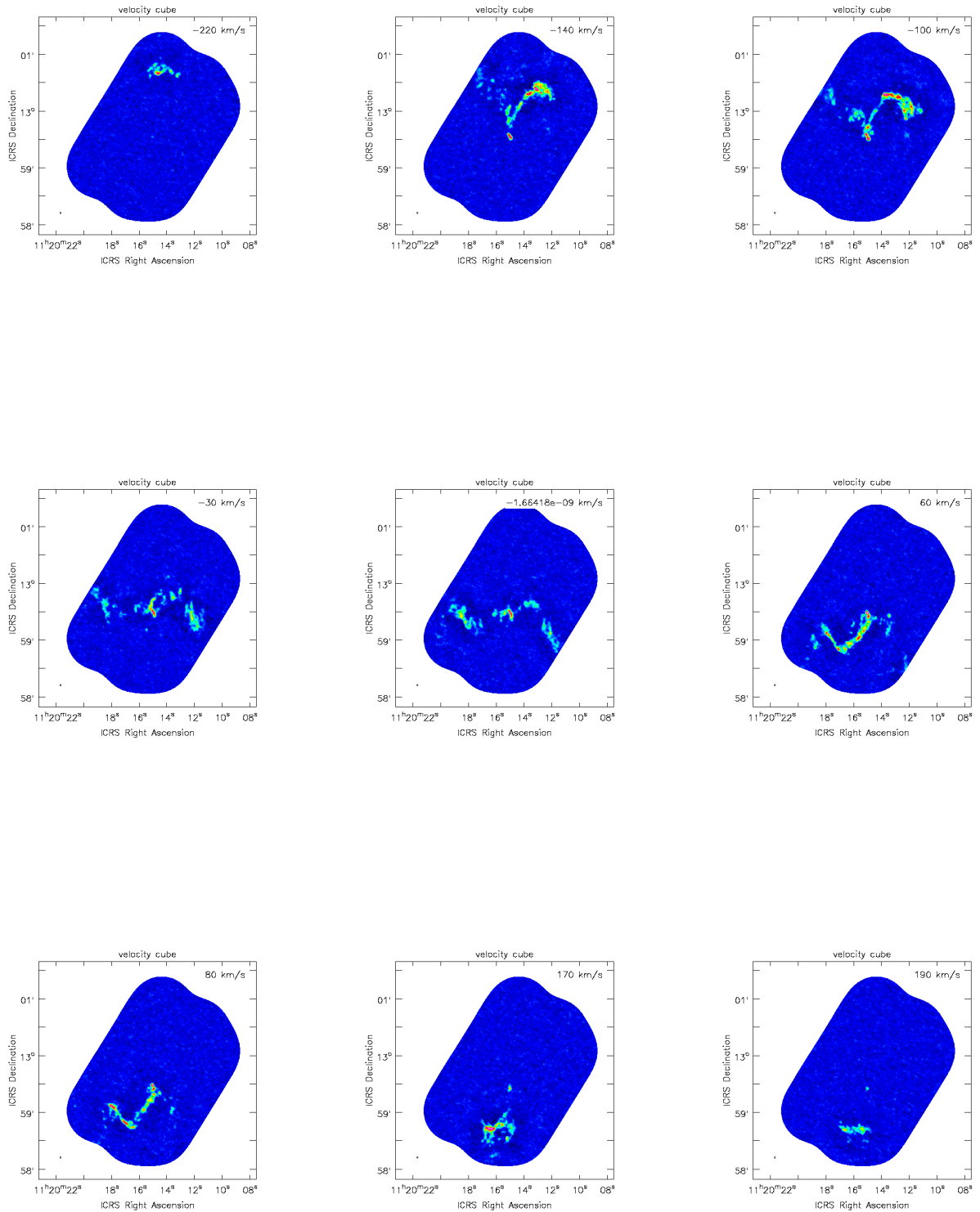


Figure 3.11: Some frames of the velocity cube obtained for NGC 3627. Different zones have different velocities. The synthesized beam is shown in the lower left corner of each panel, with FWHM size of  $1.667'' \times 1.511''$  and position angle of  $50.154^\circ$ .

values, angular, spatial and spectral resolutions (channel width) are given. The peak indicates the maximum pixel value in the image [Jy/beam].

Main characteristics of the images	
Angular resolution	1.60 arcsec
Spatial resolution	$\sim 90$ pc
RMS Continuum	$2.5 \times 10^{-5}$ Jy/beam
Peak Continuum	$1.19 \times 10^{-3}$ Jy/beam
Channel width	10 km/s
RMS cube (each channel)	$1.5 \times 10^{-3}$ Jy/beam
Line peak	0.24 Jy/beam
Line width	470 km/s

Table 3.3: Main characteristics of the continuum image and the velocity cube. Peak indicates the maximum pixel value in the image.

### 3.4 The moments calculation

We use the line images to derive information about the source emission and its kinematics. We extract the moment of order 0 (line intensity), the moment of order 1 (mean velocity) and the moment of order 2 (velocity dispersion). For this we use the *immoments* task, which implements the moment formulas numerically (Eq. 3.2 and 3.3). The main parameters for this task are the channels where the emission line is actually present. We also need to define a flux threshold, which is the limit within which the algorithm will operate, given by  $5\sigma_{RMS}$ .

**Moment of order 0:** Represents the intensity of the integrated line over all velocities. Namely:

$$Mom0 = \int S_v dv \quad (3.2)$$

**Moment of order 1:** Represents the intensity weighted velocity field at each point across all observed channels:

$$Mom1 = \langle V \rangle = \int \frac{S_v v dv}{S_v dv} \quad (3.3)$$

**Moment of order 2:** It weights the spectral intensity contributions by the square of the difference between the velocity at each point in the spectrum and the systematic velocity of the source (Eq. 3.4). This moment provides information about the velocity dispersion in a region.

$$Mom2 = \langle V^2 \rangle^{1/2} = \int \frac{(v - \langle V \rangle)^2 S_v dv}{S_v dv} \quad (3.4)$$

The images obtained from the calculation of moments are given in the next chapter (Fig. 4.2, 4.3 and 4.4 in Section 4.1).

### 3.5 Ancillary data

The  $H\alpha$  image and the corresponding error map used to estimate the SFR in NGC 3627 (shown in Fig. 3.12) are from the MUSE-PHANGS survey [21], which is a key part of the PHANGS project.

The footprint of the PHANGS-MUSE survey was designed to overlap with the area of the sky imaged by PHANGS-ALMA in CO(2-1), which should include all regions of active star formation within the disk. The mosaic covering NGC3627 is composed of 8 individual MUSE pointings.

Detailed information on the data reduction and analysis process is given in Emsellem (2022)[21]. We have downloaded the NGC3627 MUSE datacube from the PHANGS archive<sup>2</sup>. The cube is corrected for foreground galactic extinction as in the stellar continuum fit performed on individual three-dimensional pixel. The cube was convolved and optimized at a resolution of 1.05 arcsec. Convolution and optimization allow to homogenize the point spread functions, which vary over the spatial field of view due to the combination of multiple individual pointings, and to obtain a wavelength independent circular Gaussian PSF. An adapted resolution extinction correction (described in Pessa et al. 2021[48]) makes the PHANGS-MUSE dataset suitable for robust SFR estimation.

In order to determine the SFR, we used the assumptions described in the section 1.3.1. The MUSE image has been regridded to the same geometry as the ALMA mosaic.

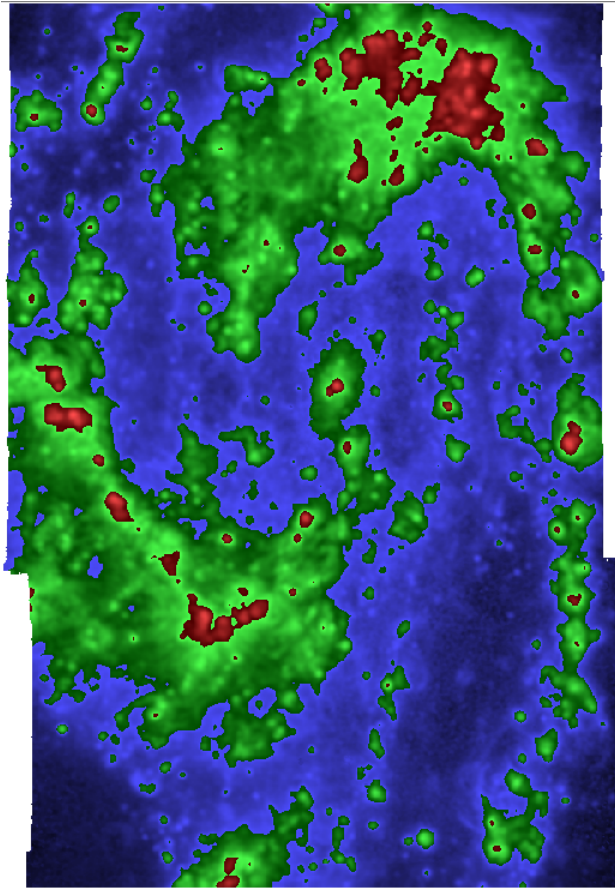


Figure 3.12:  $H\alpha$  map of NGC 3627 from MUSE observations

<sup>2</sup><https://www.canfar.net/storage/vault/list/phangs/RELEASES/PHANGS-MUSE>

# Chapter 4

## Analysis and results

Using the obtained CO images we determined the total molecular mass of NGC3627 and the physical properties of GMCs in different environments of the galaxy. To identify the GMCs we used the software Astrodendro.

The surface density of molecular gas in the identified GMCs was calculated. In addition, the surface densities of the SFRs were calculated from the H $\alpha$  emission map of the same galaxy. These two results were then compared to study the Kennicutt-Schmidt law, at the spatial scale of  $\sim 90$  pc.

Our study was centered on the examination of GMCs within various subregions (galactic structures or environments) of NGC 3627, including the core, bar, bar ends, galactic disk, intra-arm regions, and spiral arms. The classification of these subregions was derived from the prior work of Querejeta et al. (2021). [49]

### 4.1 Molecular gas in NGC3627

We measured the molecular mass inside an elliptical region  $165 \times 195$  arcsec in size, which encompasses the entire visible galaxy. The spectrum extracted from this region shows a broad CO(1-0) line (4.1), covering a velocity range of  $\sim 400$  km/s, representing the total velocity dispersion of the galaxy. The line shows a double peak, which, as already discussed, tells us that the galaxy is rotating.

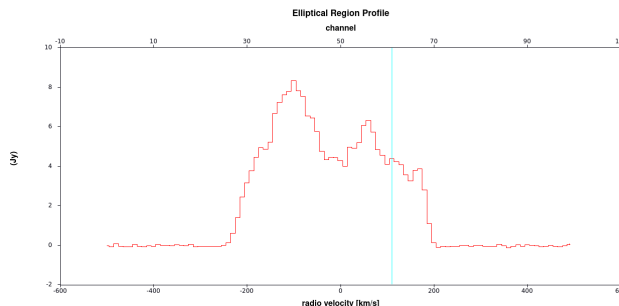


Figure 4.1: Spectrum in velocity of the CO(1-0) line obtained from the velocity cube. It shows a broadened profile and a double peak, as observed earlier (Fig. 3.9)

From the integrated intensity in this region:

$$A = \int_{v_i}^{v_f} S_\nu \Delta v \quad (4.1)$$

and multiplying it by the conversion factor (Eq. 1.4 in Section 1.2.1), we obtained an estimate of the total mass of molecular gas present in NGC 3627, which corresponds to  $M_{mol}^{TOT} \simeq (1.6 \pm 0.2) \times 10^9 M_\odot$ .

From the CO(1-0) moments images described in Section 3.4, we can obtain some properties of the molecular gas distribution in the galaxy:

- In the **Moment 0** image (Fig.4.2) we can see how this intensity follows the trend of the arms and highlights the different structures of the galaxy, such as the bar and the nucleus. We observe knots of strong emission at the north and south bar ends, as well as an additional knot (structured, not monolithic) at the core.
- The **Moment 1** image (Fig. 4.3) unveils significant kinematic structure by highlighting intensity-weighted peak velocities in the regions of interest. We notice a rotational motion of the galaxy, in our case using the velocity of the central part as a reference (to zero), and we see that the northern part has negative velocities and the southern part positive. The western arm displays the largest gradients, with velocities ranging from -200 km/s to  $\sim +100$  km/s. The eastern arm also has large gradients, with velocities ranging from -50 km/s to  $\sim +150$  km/s.
- Finally, the **Moment 2** (Fig. 4.4) shows us that the core is the zone with the highest velocity dispersion (in this zone the dispersion exceeds 60 km/s). Other areas with high dispersion are the bar, the bar ends (especially the southern one), and the eastern arm: in these areas, the dispersion is between 20 and 50 km/s. On the other hand, the western arm has low velocity dispersion.

## 4.2 Definition of different types of environments

This investigation utilized masks derived from a previous study by Querejeta et al. (2021)[49], where morphological structures and environments within the PHANGS sample of 74 nearby galaxies were discerned through Spitzer 3.6  $\mu\text{m}$  observations. These masks facilitated a subregion-level analysis, defining structures such as the disk, bar, and spiral arms. The disk was identified through photometric decomposition of near-infrared images, the bar through elliptical fitting and comparison with known barred galaxies, and spiral arms through peak identification on unsharp-masked 3.6  $\mu\text{m}$  images, followed by log-spiral fits in polar coordinates, with a width empirically established based on the spatial distribution of CO emission. In this work, each pixel is assigned to only one zone, and the masks have a characteristic pixel value ranging from 1 to 7 (1-6 for different galactic structures, 7 for areas outside the galaxy). The mask that corresponds to NGC 3627 is shown in Fig. 4.5.

Under this mask, NGC 3627 is divided into 6 zones: two spiral arms (east and west, colored pink in Fig. 4.5), a galactic bar (dark green) with the core (purple) in the center and the bar ends (north and south; light green) at its ends. Surrounding the bar is the galactic disk (dark khaki), from which two spiral arms (east and west; pink) extend. By intra-arm region we mean the regions at the boundary between the disk and the spiral arms (orange).

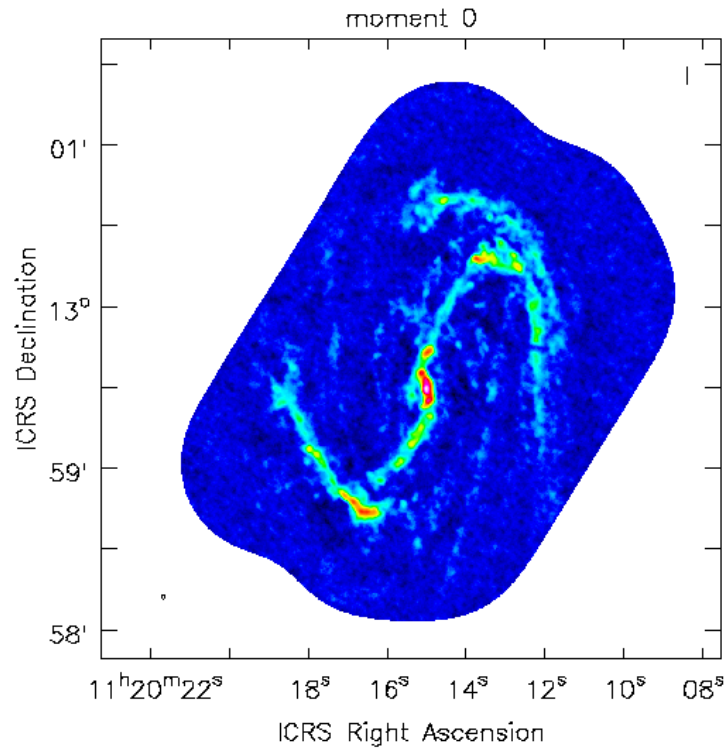


Figure 4.2: Moment 0 image of the final image. The structures of the galaxy, including the core, bar, and arms, are visible. The synthesized beam is shown in the lower left corner, with FWHM size of  $1.667'' \times 1.511''$  and position angle of  $50.154^\circ$ .

### 4.3 GMCs identification

The angular resolution we have allows us to obtain spatial resolutions of  $\sim 90$  pc, which allows us to study GMCs. In addition, the masks described in the previous section allowed us to study the properties of molecular clouds in different galactic environments.

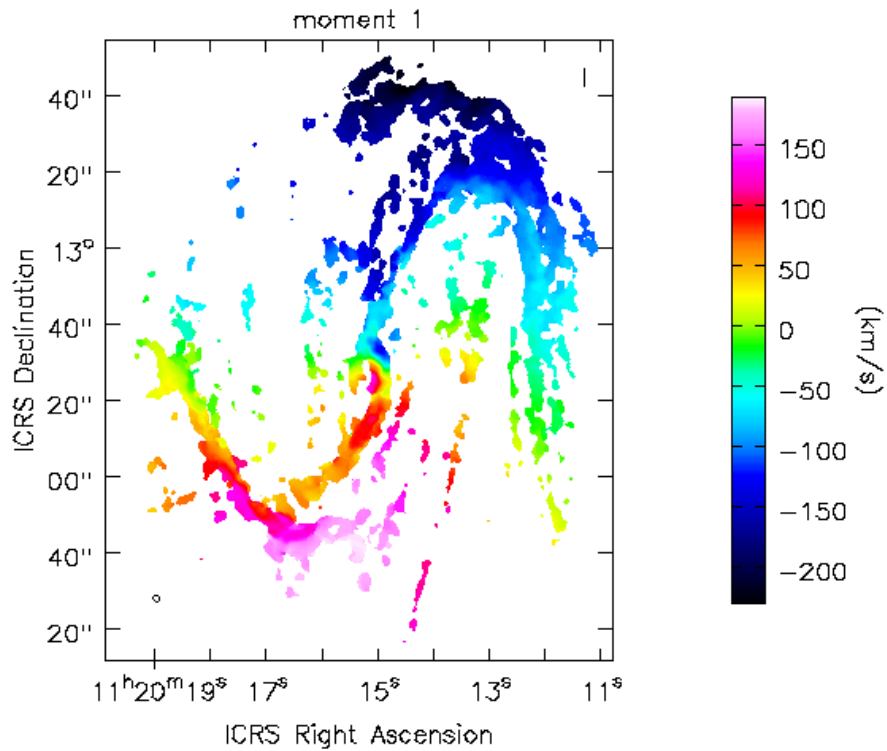


Figure 4.3: Image of the moment of order 1 of the three datasets combined. Blue shading indicates negative velocities (i.e., approaching on the line of sight). The northern part of the galaxy is approaching on the line of sight. The southern part is receding. The synthesized beam is shown in the lower left corner, with FWHM size of  $1.667'' \times 1.511''$  and position angle of  $50.154^\circ$ .

The identification of the GMCs was done using the Astrodendro tool, from the zero moment image of NGC 3627 (obtained in section 3.4).

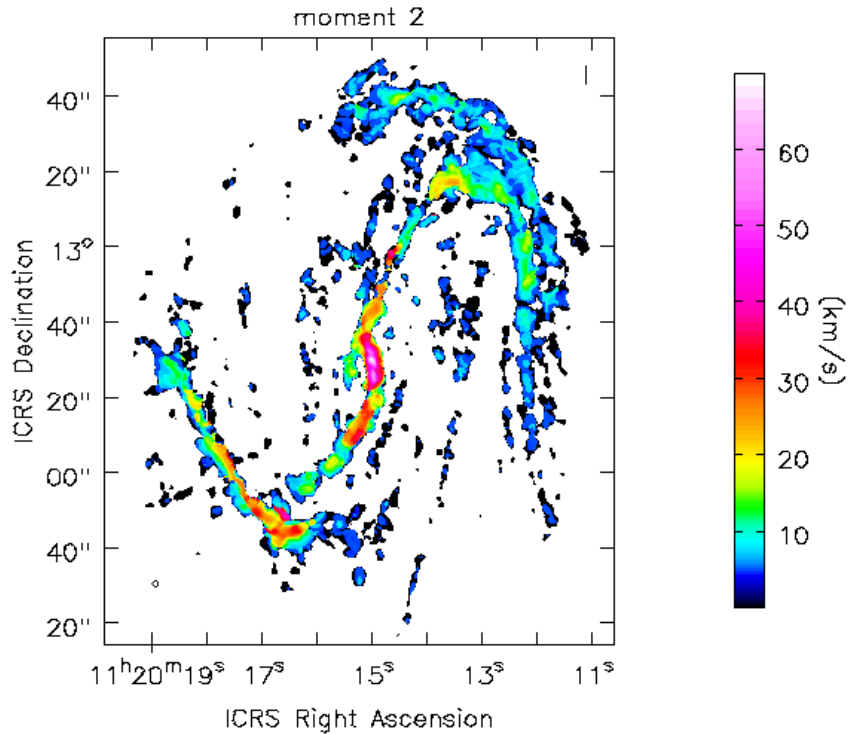


Figure 4.4: Image of moment 2. The largest velocity dispersions are found in the bar. Other areas of high dispersion are the bar, the bar ends (especially the southern one), and the western arm. The synthesized beam is shown in the lower left corner, with FWHM size of  $1.667'' \times 1.511''$  and position angle of  $50.154^\circ$ .

### 4.3.1 Astrodendro

Astrodendro<sup>1</sup> is a software written in Python that generates dendrograms for exploring and displaying hierarchical structures in observed or simulated astronomical data. It handles noisy data by allowing specification of the minimum height of a structure and the minimum number of pixels required for an independent structure. Using the astrodendro package is quite simple and gives us an interactive view of the generated dendrograms [51].

<sup>1</sup><https://dendrograms.readthedocs.io/en/stable/index.html>

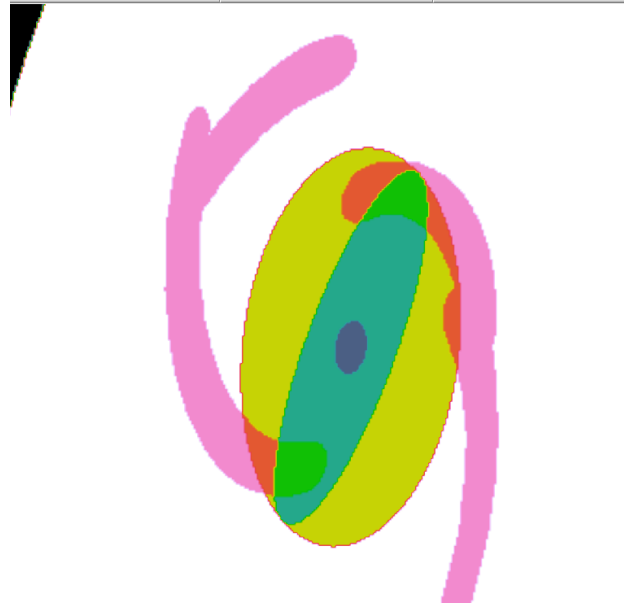


Figure 4.5: Image of the various substructures of NGC 3627 identified from Querejeta et al. (2021). Each zone (substructure) has a characteristic pixel value: Core=1 (in purple in figure), bar=2 (green), bar ends=3 (light green), disk=4 (dark khaki), intra-arm=5 (orange), arms=6 (pink).

The simplest way to think of a dendrogram is as a tree structure that represents the hierarchy of structures in the data. A dendrogram comprises two distinct elements: *branches*, representing structures that divide into multiple sub-structures, and *leaves*, denoting structures without any sub-structure. Branches can further divide into branches and leaves, enabling the effective representation of hierarchical structures. The term *trunk* is employed to describe a structure without a parent structure. In other words (as shown in the Fig. 4.6), the primordial structures are the trunks, and the ultimate structures are the leaves, while the intermediate structures are the branches.

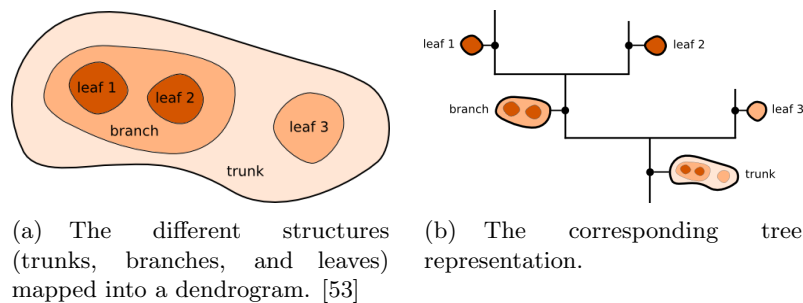


Figure 4.6: Dendrogram representation [52]

In our case, we constructed our dendrogram from the zero moment image (Fig. 4.2). The algorithm starts with the brightest pixel in the image. The first structure is generated from this pixel. It then proceeds to the pixel with the next highest value. At each step, a decision is made whether to integrate the pixel into an existing structure or to create a new structure. A new structure is created only if the value of the pixel exceeds that of its immediate neighbors, which is called a local maximum. The algorithm continues to move toward less bright pixels until it finds a pixel that is not a local maximum and is adjacent to both peaks: at this point, the two peaks

are merged, i.e., a branch is created. As the algorithm moves to less bright pixels, the structures merge to form the tree.

The algorithm continues until a minimum flux value is reached, which is defined by the ‘min value’ parameter and chosen based on the noise of our data (Fig. 4.7). The other important parameter for the construction of a dendrogram is ‘min delta’, which is the step by which the software makes its descent into the flux. A structure is included in the tree only if its height exceeds a minimum value defined by min delta. This parameter allows us to avoid including structures that are really just noise. Choosing a too-high a value of this parameter can cause us to miss certain leaves.

In our case, we chose a minimum value of  $0.5 \text{ Jy} \cdot \text{km/s}$ , which is slightly more than twice the RMS of the moment 0, and  $0.1 \text{ Jy} \cdot \text{km/s}$  as the ‘min delta’ value.

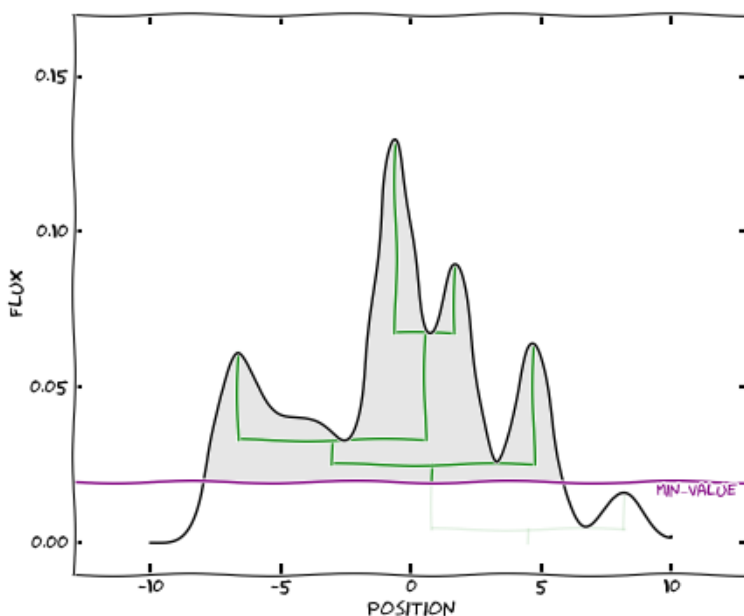


Figure 4.7: Process of identifying local maxima (i.e. structures) of Astrodendro. The process stops when a minimum flux value specified by the min value parameter is reached. [53]

#### 4.4 Characterization of the detected GMCs

As mentioned above, we performed the dendrogram construction from the zero-moment image. The images that we imported are in *.fits* format. Astrodendro derived the tree structure (Fig. 4.8) and initially identified 882 leaves.

We created an image where all pixels within a given leaf are identified by an index, and saved this mask in a new *.fits* file. This will allow us to associate the leaves found by Astrodendro with molecular emission substructures, and in certain instances, we will be able to correlate them with GMCs.

Despite a signal-to-noise ratio  $(S/N) > 2$ , the possibility of false detections among the identified clouds exists. To address this, a visual inspection of the zero-moment image and the velocity cube

was conducted at the locations where clouds were identified. Figure 4.10 provides a clearer view, superimposing identified clouds on the zero-moment image of NGC 3627.

Upon examination of the velocity cube, it was observed that some identified features did not align with structures classifiable as clouds, as genuine clouds are expected to span at least 3 velocity channels. These features are treated as noise. Additionally, certain potential clouds identified from moment zero were found to be located outside of any structure in the galaxy, as illustrated in Fig. 4.11. Such clouds were excluded.

Following this filtering process, 552 clouds remained, and these selected clouds are considered Giant Molecular Clouds (GMCs) in the scope of this study.

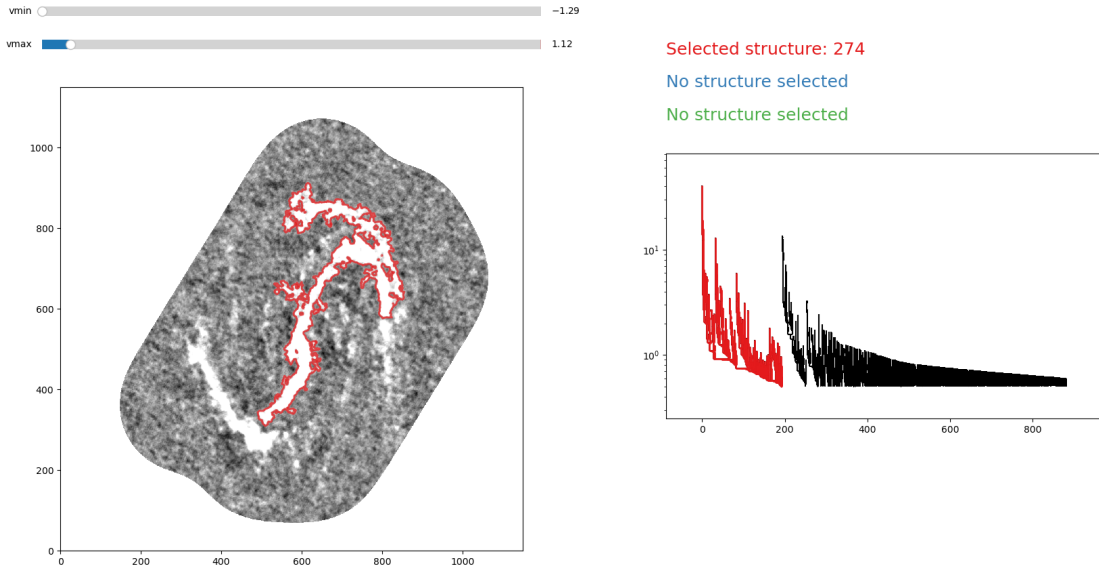


Figure 4.8: Dendrogram generated from the zero-moment image. On the left the structures found in the image of NGC 3627 are reported, on the right the corresponding tree structure is shown. To give an example of the structure of the dendrogram, we can see the red region in the image of the galaxy, which corresponds to a single trunk of the dendrogram (highlighted in red, in the figure to the right).

For all detected leaves, Astrodendro gives us CO flux (in Jy), exact two-dimensional area (in square arcsec), pixel position, position angle.

From the estimate CO(1-0) emission flux of the clouds, we obtained their molecular masses through a conversion factor (see equation 1.4 in Section 1.2.1). As a measure of the distance  $D$  we use  $10.6 \pm 0.6$  Mpc[36]. We also use this distance to convert cloud surface measurements from square arcseconds to square parsecs.

#### 4.4.1 GMC masses and mass distribution

Figure 4.12 shows the histogram of the identified GMC. The cloud masses found ranged from  $10^4$  to  $10^8 M_{\odot}$ . The peak of the distribution is around  $\sim 10^5 M_{\odot}$ . The distribution is mainly concentrated between  $10^5$  and  $10^6 M_{\odot}$ . The distribution decays smoothly as we go to higher masses, with extreme elements having masses  $\sim 10^8 M_{\odot}$ , which are probably blending between multiple clouds and not

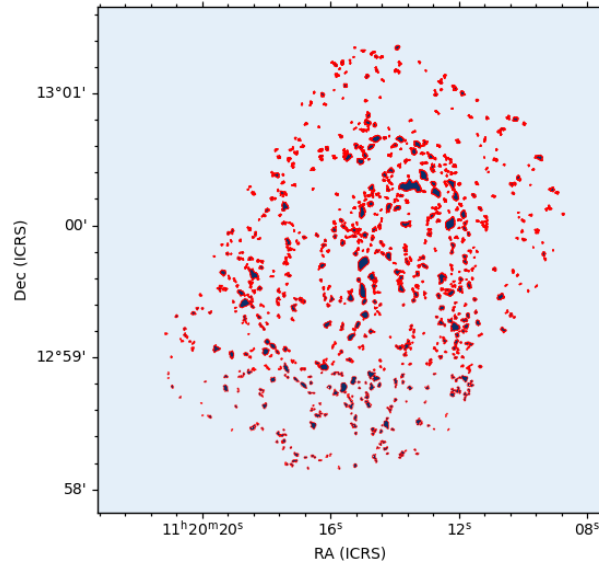


Figure 4.9: Structures identified as GMC in NGC 3627 using Astrodendro

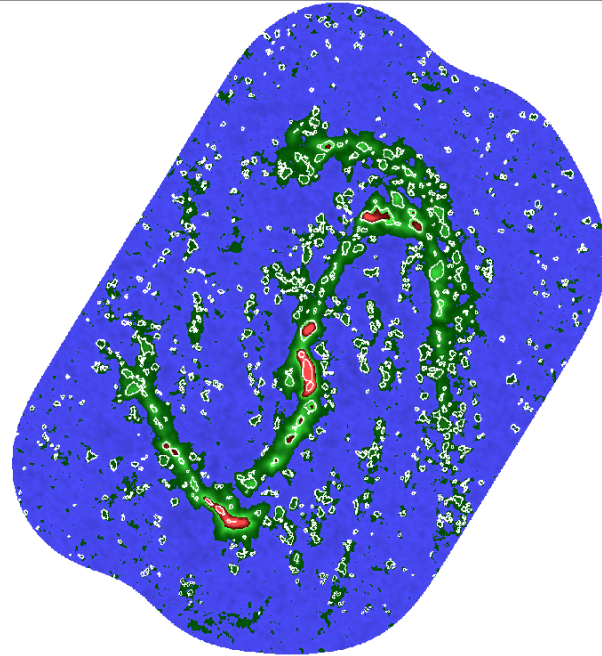


Figure 4.10: The structures identified as GMC (white contours) superimposed on the (moment zero) image of NGC 3627

individual GMCs. In general, the most massive GMC are found in the central regions (central regions of the bar and core).

We found that the clouds we identified as GMC in NGC 3627 have an average mass  $M_{\text{Mean}} \sim (1.5 \pm 0.2) \times 10^6 M_{\odot}$ . While the total sum of their masses gives a  $M_{\text{TOT}}^{\text{GMC}} \approx (8.1 \pm 0.3) \times 10^8 M_{\odot}$ .

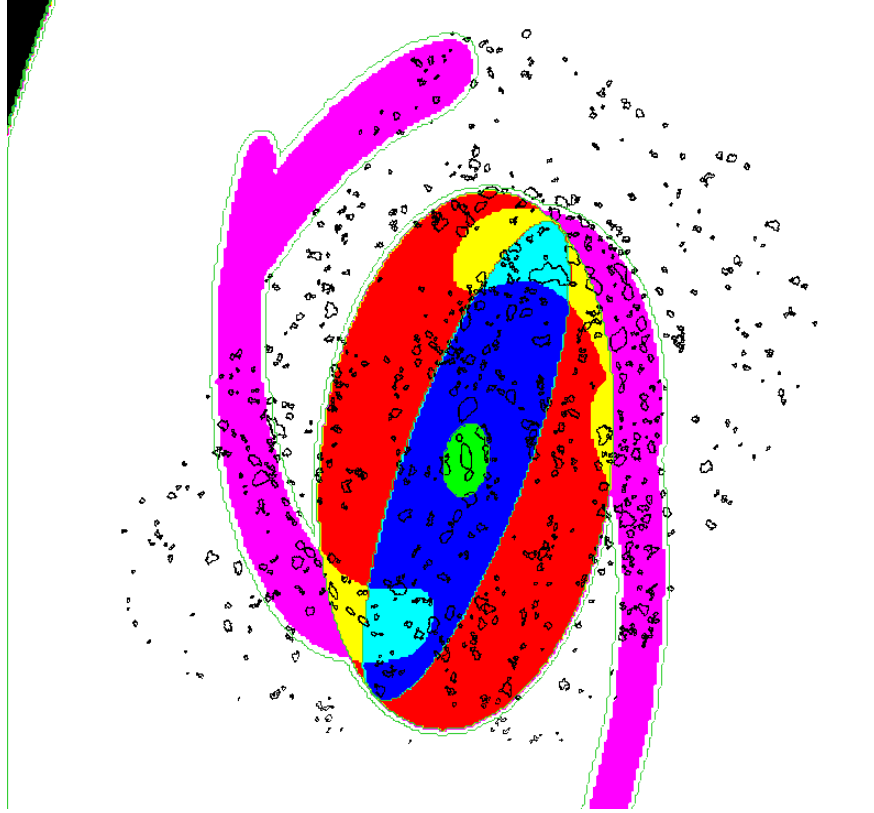


Figure 4.11: Overlay of the clouds we identified with masks of the different substructures of NGC 3627 obtained from Querejeta et al. 2021. Note that some of the “clouds” we obtained are located outside the galactic regions and have therefore been discarded.

The measurement, despite being of a comparable order of magnitude, proves to be smaller than the total molecular mass estimate derived from the CO(1-0) line broadening (section 4.1). This fact tells us that we are including regions not identified by Astrodendro when we integrate the spectrum. With our method we are missing a non-negligible fraction of molecular gas in the form of clumps or clouds.

This mass distribution of GMCs was also studied at the level of morphological structures by applying the masks described in the previous section. The reader will notice that the sum of GMCs in the structures (708) is larger than the number of identified GMCs (552). This is due to the fact that some individual clouds are arranged along multiple structures, so they are counted multiple times. In Fig. 4.11 we can see, for example, that certain bar clouds overlap with either a bar end or the core; or that certain clouds within the spiral arms are also part of the intra-arm region. The histograms corresponding to each environment are shown in Fig. 4.13.

**Galactic bar:** The main morphological feature of NGC 3627 is the presence of a bar. We identified **130 clouds present in the bar**, which gives us a mass distribution as shown in the green histogram in Figure 4.13. The peak of the distribution is on the order of  $1.5 \times 10^5 M_{\odot}$ . Most of the clouds have masses between  $10^5$  and  $10^6 M_{\odot}$ , with 3 cases of the order of  $10^7 M_{\odot}$ . These more massive clouds are found in the central part of the bar, near the core (as can be seen in Fig. 4.14). We find that the average mass of the bar’s GMCs is  $M_{Mean} \sim (1.32 \pm 0.20) \times 10^6 M_{\odot}$ .

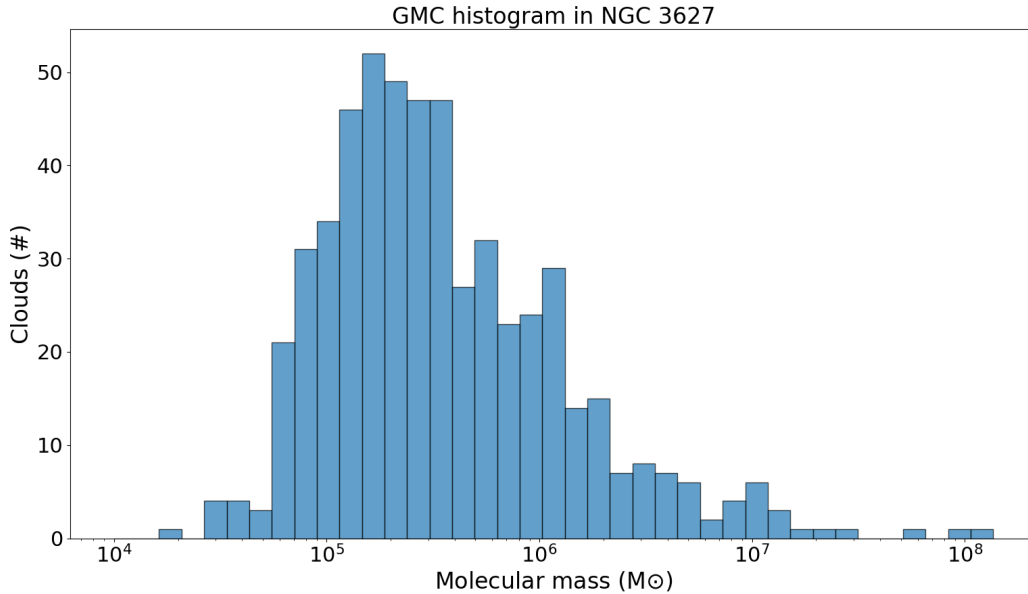


Figure 4.12: Mass distribution of the detected GMCs. On the abscissa we have the masses of our clouds divided into 40 bins, and on the ordinate the number of clouds per mass bin.

**Bar ends:** We identified **36 GMCs** in these zones (northern and southern bar ends). The mass distribution of these clouds is shown in the blue histogram in Figure 4.13. The peak of the distribution is about  $2 \times 10^5 M_{\odot}$ . Almost all clouds have masses between  $10^5$  and  $10^6 M_{\odot}$ , with 4 cases having masses  $\sim 10^4 M_{\odot}$ . The average mass of GMCs identified in this areas is  $M_{Mean} \sim (3.32 \pm 0.50) \times 10^6 M_{\odot}$ .

**Disc:** Here we found **169 GMCs**, with a distribution as shown in the yellow histogram of Figure 4.13. The peak of the distribution is about  $2 \times 10^5 M_{\odot}$ , and the masses of the GMCs range between  $10^5$  and  $10^7 M_{\odot}$ , decreasing in number from  $10^6 M_{\odot}$ . The three most massive clouds in the disk are located in the northern zone, not far from each other (Fig. 4.14). Also, the average mass of GMCs identified in the disc is  $M_{Mean} \sim (5.34 \pm 0.81) \times 10^6 M_{\odot}$ .

**Intra-arm regions:** In the structure we found **38 GMC**, distributed in terms of mass as shown in purple in Figure 4.13, where we note that the most common mass value is  $\sim 2.5 \times 10^5 M_{\odot}$ . The distribution ranges from  $10^4$  to almost  $10^7 M_{\odot}$ . The average mass of the GMCs identified in these areas is  $M_{Mean} \sim (1.33 \pm 0.20) \times 10^6 M_{\odot}$ .

**Spiral arms:** In NGC 3627 we have two spiral arms (north and south). A total of **193 GMC** have been detected in these regions, distributed (in mass) as shown in cyan in Figure 4.13. The peak of the distribution is about  $2 \times 10^5 M_{\odot}$ . Spiral arms, together with the bar, are the environments where we find the widest mass ranges: the clouds have masses between several  $10^4 M_{\odot}$  and a few  $10^7 M_{\odot}$ , although the bulk of the mass distribution is between  $10^5$  and a few  $10^6 M_{\odot}$ . The average mass of these clouds is  $M_{Mean} \sim (1.00 \pm 0.15) \times 10^6 M_{\odot}$ .

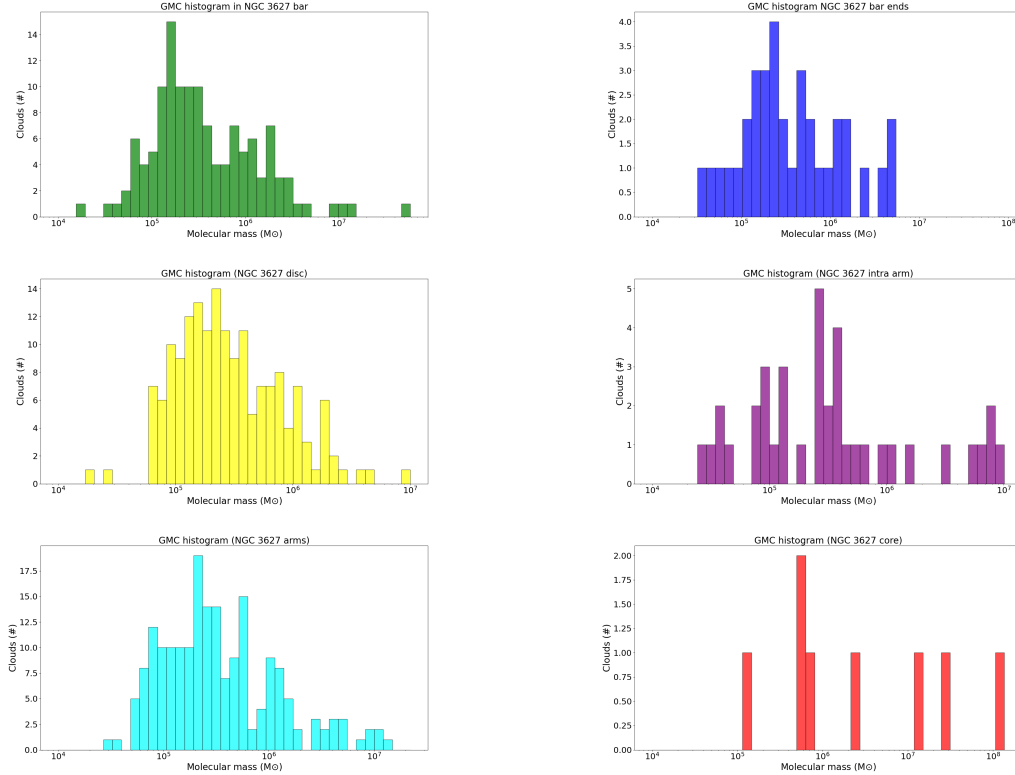


Figure 4.13: Histograms showing the mass distribution of GMCs in each environment. From left to right and top to bottom: bar, bar ends, disk, intra-arm, spiral arms and core.

**Core:** In the core, the statistics we have are poor. In fact, we found only 8 clouds, distributed in mass as shown in red in Fig 4.13. Here we note one cloud with a particularly high mass ( $\sim 10^8 M_{\odot}$ ): Located in the very central zone of NGC 3627, this cloud is the most massive of all the clouds we have identified in the galaxy (Fig. 4.14).

In Figure 4.14, the most massive GMCs in each environment are indicated by red and black dashed circles (for the core and bar ends, we have highlighted only the most massive; for the other areas, the 3 most massive). The most massive clouds we found in NGC 3627 are those in the central zones belonging to the core and the bar.

## 4.5 SFR

From the H $\alpha$  maps described in section 3.5, we determined the luminosity  $L_{H\alpha}$  in the regions of the map corresponding to the CO identified GMCs, thus obtaining an estimate of the SFR for each of our clouds. By relating the masses of the GMCs to their respective SFRs, we obtained a scatter plot as shown in Figure 4.15, from which we calculated the following relationship:

$$\log_{10}(SFR) = (0.83 \pm 0.04)\log_{10}(M_{mol}^{GMC}) - (5.94 \pm 0.20) \quad (4.2)$$

It is clear from Fig. 4.15 that the most massive clouds are more active in star formation.

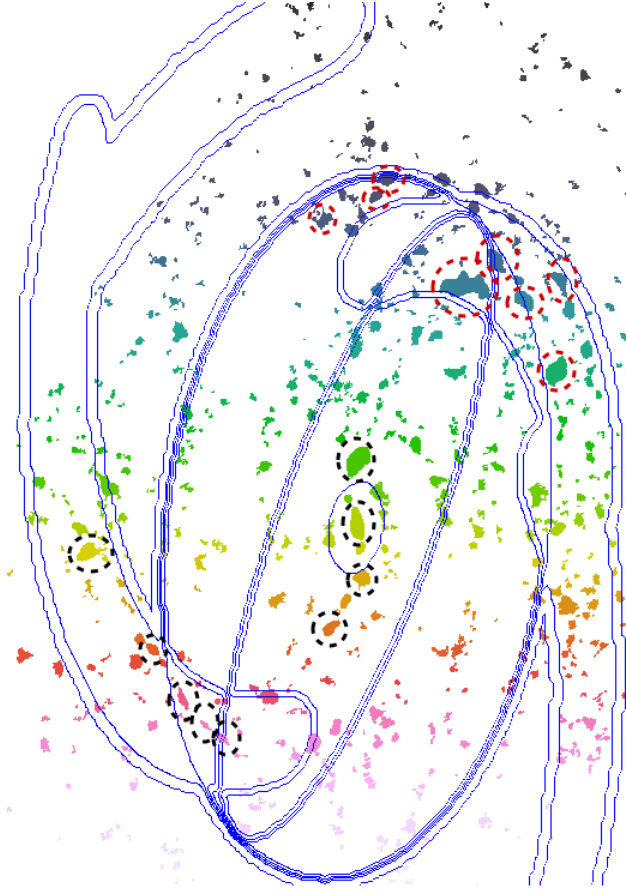


Figure 4.14: Most massive GMC in each environment (red a black dashed circles). For the core and bar ends, we have highlighted only the GMC most massive; for the other areas, the 3 most massive. The most massive GMCs in NGC 3627 are in the central zones.

## 4.6 Kennicutt-Schmidt Law in NGC 3627

We also obtained the surface SFR ( $\Sigma_{SFR}$ ) for each of our GMCs and related it to their respective surface molecular mass densities ( $\Sigma_{M_{mol}}$ ) in a scatter plot like the one shown in the Figure 4.16, where we can observe different colors for the GMCs depending on the morphological structure they occupy in the galaxy. At first glance, we observe that the clouds with the highest values of both  $\Sigma_{SFR}$  and  $\Sigma_{M_{mol}}$  are located in the core. Additionally, there is a notable concentration of points around  $\Sigma_{M_{mol}} \sim 10^2 M_{\odot}/pc^2$ .

A linear fit was performed on this scatter plot to obtain a Kennicutt-Schmidt type relationship (Fig. 4.17). On a global scale, i.e. considering all the 552 clouds we selected, the relationship found was:

$$\Sigma_{SFR} \approx 10^{(-3.17 \pm 0.19)} \times (\Sigma_{M_{mol}})^N, \text{ with } N = 0.86 \pm 0.09 \quad (4.3)$$

KS type relationships were also obtained for individual morphological structures. The KS indexes obtained are shown in Table 4.1, as well as the intercepts, while the plots of the different regions are shown in the next section, in Figure 4.19. The region with the highest KS index is the galactic disk. In this region, the obtained KS law exhibits a steeper slope compared to that of the entire galaxy. Other regions, such as the spiral arms, also show a pronounced slope, surpassing that

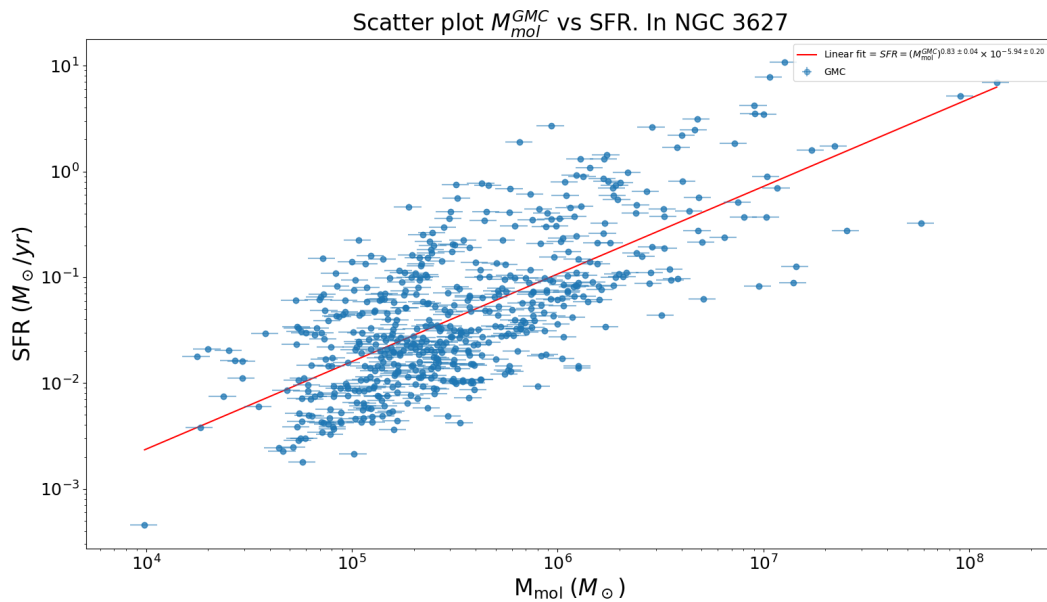


Figure 4.15: Scatter plot between the masses of our GMCs and their respective SFRs obtained from the luminosity  $H\alpha$ .

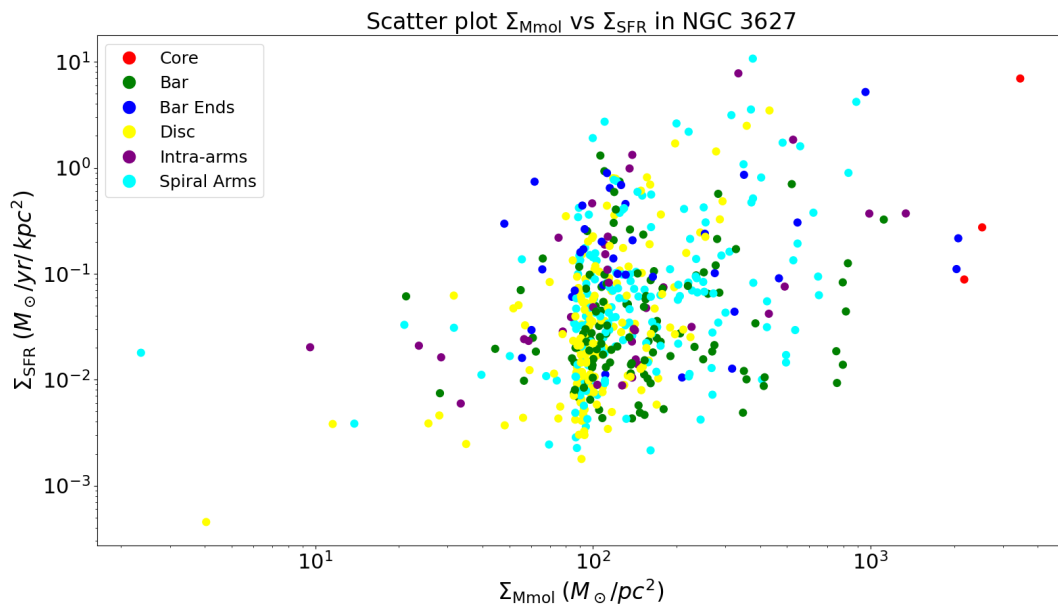


Figure 4.16: Graph showing the surface gas density of our GMCs versus their surface SFR. The colors indicate the environment in which our clouds are located.

of the overall galaxy. It should be reported that 16 of the identified GMC in the spiral arms had no visible counterpart in the  $H\alpha$  emission map. These clouds were not included in the determination of this relationship.

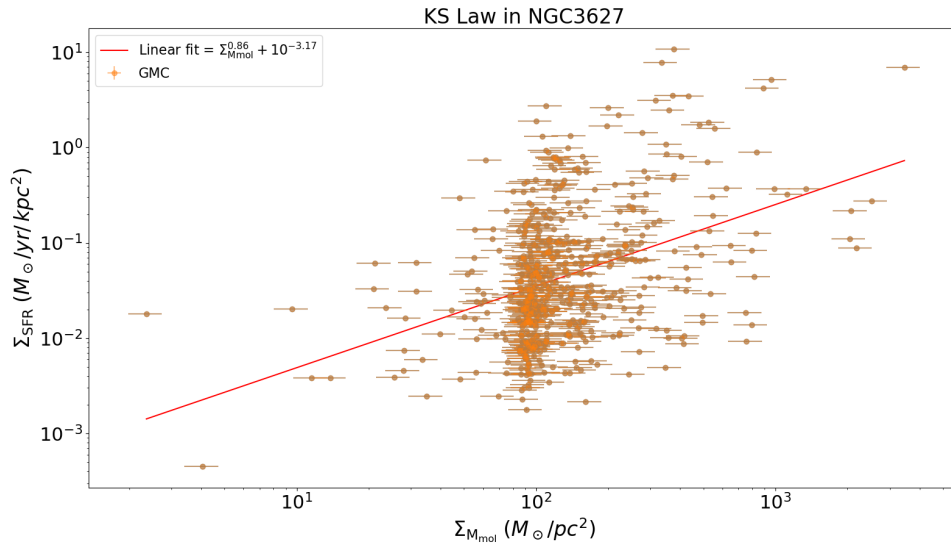


Figure 4.17: Kennicutt-Schmidt type relation for clouds scattered throughout the galaxy. KS index  $N = 0.83 \pm 0.09$ .

Environment	Number of GMC	Mean $M_{mol}$ ( $\times 10^6 M_{\odot}$ )	KS index $N$	Intercept (log)
Bar	130	$1.32 \pm 0.20$	$0.30 \pm 0.13$	$-2.10 \pm 0.27$
Bar ends	36	$3.32 \pm 0.50$	$0.08 \pm 0.21$	$-1.02 \pm 0.46$
Disc	169	$0.53 \pm 0.08$	$1.23 \pm 0.17$	$-4.00 \pm 0.34$
Intra-arms	38	$1.33 \pm 0.20$	$0.78 \pm 0.19$	$-2.73 \pm 0.40$
Arms	193	$1.00 \pm 0.15$	$0.90 \pm 0.16$	$-3.18 \pm 0.35$
Total galaxy	552	$1.46 \pm 0.22$	$0.86 \pm 0.09$	$-3.17 \pm 0.19$

Table 4.1: Number of clouds, average  $M_{mol}$ , KS index ( $N$ ) and the intercept with  $y$ -axis ( $\Sigma_{SFR}$  axis) for each environment and for NGC 3627 as a whole (total galaxy).

The intraarms and the core presents very similar slopes to each other, both slightly smaller than the entire galaxy.

A separate discussion is warranted for the bar, where the slope is relatively flat, and even more so in the bar ends, where  $N$  is close to zero.

## 4.7 Comparison with previous results

The data obtained are found to be consistent with the results of previous work. However, in some cases we find significant differences. This is the case with the work of Rosolowsky et al. 2021 [54] in which they identified 1048 GMCs in NGC 3627, almost twice as many as we identified. This is due to the different clouds identification method used; we identified GMC from the moment 0 image, obtained including only emission above the threshold mentioned in section 3.4, instead of velocity cube. Although our GMCs are in the mass range of Rosolowsky's, we do have some clouds with larger masses ( $\sim 10^8 M_{\odot}$ ) found in the core and central parts of the bar, where astrodendro identified as single clumps regions where many are possibly blended. A more accurate

GMC identification in the cube image can improve the results.

However, it should be noted that Rosolowsky’s observations are made in the CO(2-1) band, which detects zones of molecular gas that tend to be denser than those detected by CO(1-0). As for the  $\Sigma_{M_{mol}}$ , our clouds fall within the range found in the previous work ( $10^1$  to  $\lesssim 10^3 M_{\odot}/pc^2$ ), with certain cases above, which can always be associated with central clouds. Regarding the  $\Sigma_{M_{mol}}$ , Sun et al. 2018 calculated this value for a sample of 15 spiral galaxies where NGC 3627 is not present. The values they obtained are slightly lower than ours, with maximum  $\Sigma_{M_{mol}}$  values of  $\sim 200 M_{\odot}/pc^2$ .

The KS we obtained on the whole galaxy is in agreement (within the errors) with the result obtained by Querejeta et al. 2021 [49] on a sample of 74 galaxies, including NGC, using observations of CO(2-1) line emission. The comparison is shown in Figure 4.18. Querejeta studied the KS in galactic subregions as well: the green dashed lines shown in the graphs in Figure 4.19 represents the KS laws for each environment, averaged over the entire sample. Our results in the intra-arm, core, disk, and spiral arms are in agreement within the errors with [49]. However, in the bar and bar ends, our KSs are much flatter (we should point out that they do not distinguish between bar and bar ends). The SFR values we find in the bar are lower. It should be noted that our statistics in the bar ends are poor because of the few clouds we encounter (only 36).

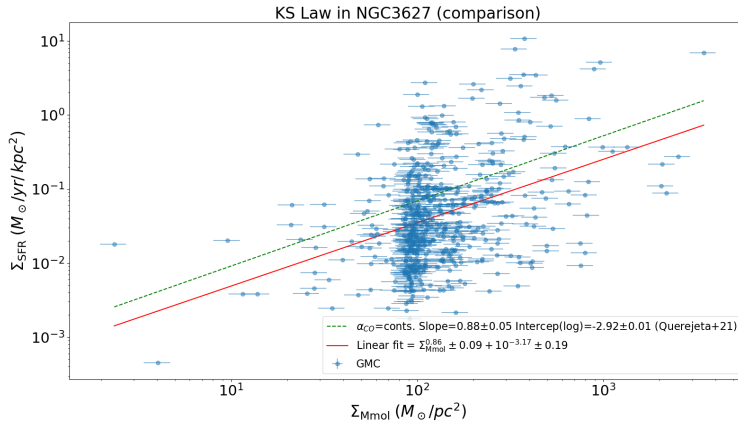


Figure 4.18: Comparison between the KS law in NGC 3627 determined by us (red line) and the KS obtained by Querejeta et. al (2021) on a sample of 74 galaxies, including NGC 3627 (green dashed line).

Regarding the study of the SFR, Lada et al. 2012 [34] studied the scaling relationships between the SFR and molecular gas masses for both local galactic clouds and a sample of external galaxies. The GMCs that we identified have larger masses than those in their sample, and the relationship with the SFR we determined is in agreement with theirs, as shown in Figure 4.20, where the transparent square represents the region where our GMCs are located.

We observed that some of the GMCs we identified in the spiral arms have no counterpart in the H $\alpha$  map, suggesting that they are clouds without ongoing SF. This fact was also observed by Schinnerer et al. 2019 [56], using PHANGS-ALMA CO (2-1) observations and H $\alpha$  maps. The figure shows the overlap they found between SF regions and regions with molecular gas. Regions with CO emission but no SF are colored in dark blue, and we can see that they are mainly located in the spiral arms.

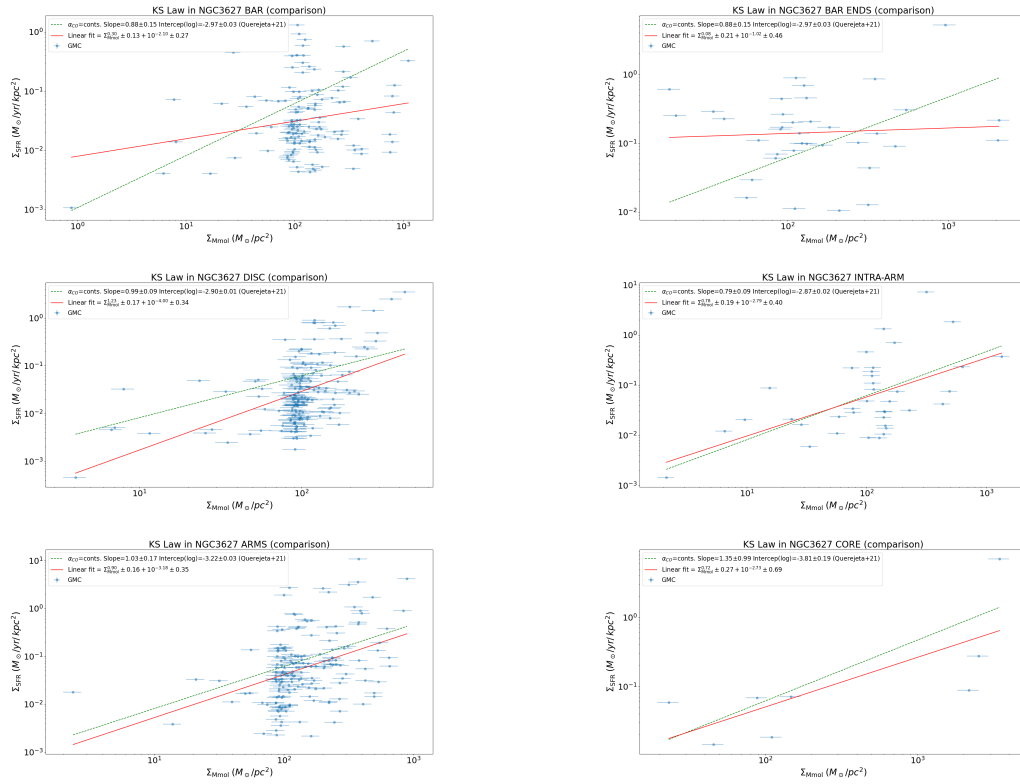


Figure 4.19: Comparison between our derived Schmidt-Kennicutt (KS) law in various environments (depicted by the red line) and the KS law obtained by Querejeta et al. (2021) across a sample of 74 galaxies, encompassing NGC 3627, environment by environment (illustrated by the green dashed line). Notably, Querejeta’s study does not differentiate between the bar and the ends of the bar. We have compared both separately with their bar. From left to right and top to bottom: bar, bar ends, disk, intra-arm, spiral arms and core.

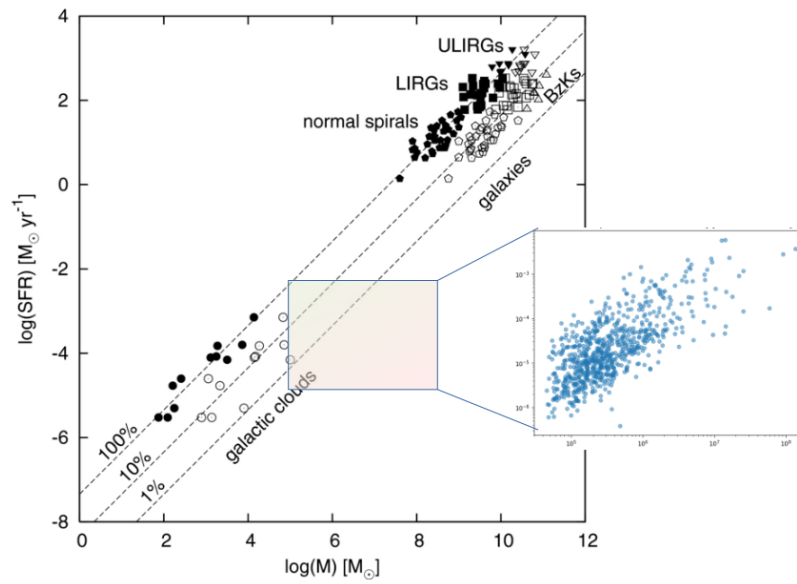


Figure 4.20: Scaling relation between  $M_{mol}$  and SFR from Lada et al. (2012). The transparent square indicates in which part of the diagram the GMCs we identified in NGC 3627 are located. The box on the right shows the  $M_{mol}$  vs. SFR pattern found for our GMCs in section

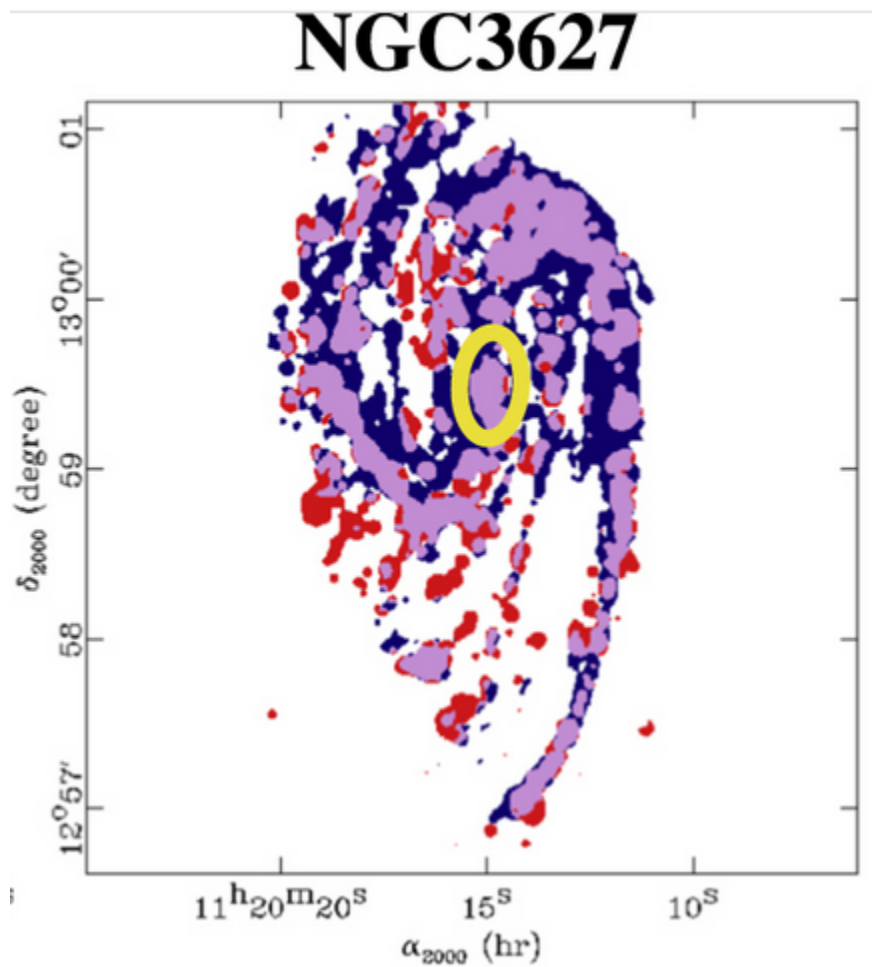


Figure 4.21: Galaxy map showing regions with overlapping CO and H $\alpha$  emission (lavender), CO only emission (dark blue) and H $\alpha$  only emission (red) at a spatial resolution of 140 pc. Yellow ellipse indicates galaxy center (Shinnerer et al. 2019).

# Chapter 5

## Summary

In the nearby Universe star formation happens in giant molecular clouds (GMC), which are dense clumps of cold gas covering size range between 10-100 pc. In order to study the connections between GMCs properties and their location inside the galaxy, it is necessary to observe large samples of galaxies, displaying different morphological structures such as bars, spiral arms, rings, circumnuclear rings. These features are connected to the galaxy evolution and possibly influence the properties of star forming gas, located in them. The use of modern observational facilities allows now unprecedented statistical studies of GMCs in nearby galaxies, exploring their multiphase ISM.

In this thesis we studied NGC 3627, a nearby barred star-forming galaxy, which allows to investigate a variety of environments, from the circumnuclear, inner and outer rings, to bar and bar ends.

Starting from ALMA observations of the CO(1-0) emission of the galaxy NGC 3627, we calibrated and imaged the data, obtaining both continuum and line images. From the line images we calculated the first 3 moments: integrated intensity, velocity and velocity dispersion; to get a more complete picture of the galaxy's emission and kinematics. The galaxy is rotating, with the northern part advancing (relative to the line of sight) and the southern part receding. The areas of the highest intensity in the line are the core and the beginning of the two spiral arms. The core is also the area with the largest velocity dispersion.

The entire galaxy has a velocity dispersion of  $\sim 400$  km/s, which can be derived from the overall broadening of the emission line. From the integrated intensity measured in an elliptical region of  $165 \times 195$  arcsec, encompassing the whole galaxy, we obtained an estimate of the total molecular mass in the galaxy:  $M_{Mol}^{TOT} \sim (1.6 \pm 0.2) \times 10^9 M_{\odot}$  (measured by conversion factor described in section 1.4).

By combining different data sets with different ALMA array configurations, we achieved an angular resolution of  $\sim 1.6$  arcsec, corresponding to  $\sim 90$  pc. This allows us to identify GMCs. Using Astrodendro (which is software that generates dendrograms that allow the study of hierarchical structures), we identify a total of 552 GMCs in the whole galaxy. For each cloud we determined the physical properties: mass, SFR, surface,  $\Sigma_{Mol}$ ,  $\Sigma_{SFR}$ . In addition, we studied the properties of clouds in different morphological structures of the galaxy.

We identified GMCs with masses in the range  $10^4 - 10^8 M_{\odot}$ , with a peak centered in  $10^{5-6} M_{\odot}$ . The regions where most GMCs are found are the disk and the spiral arms. We find that the most massive clouds ( $10^7 - 10^8 M_{\odot}$ ) are found in the central regions of the galaxy.

From the H $\alpha$  emission we obtained the SFRs and  $\Sigma_{SFR}$  for the individual clouds. This allows us to derive the relation between  $M_{mol}$  and SFR, with a slope of  $0.83 \pm 0.04$ ; and the KS law-like relation, with slope  $N = 0.86 \pm 0.09$ . The two relations are very similar, as expected, and show a

clear correlation between the amount of molecular gas in a cloud and the SFR.

The KS Law has also been determined in different regions inside the galaxy, where is found to vary from region to region. The disk is the region where we see the steepest KS, with an index of  $N = 1.23 \pm 0.17$ . Another region with a very steep index (higher than that of the whole galaxy) are the spiral arms ( $N = 0.90 \pm 0.16$ ). That indicates more stars forming for the same mass

The bar, on the other hand, has a rather flat KS-type relationship ( $N = 0.30 \pm 0.13$ ). Even flatter is the relationship obtained in the bar ends:  $N = 0.08 \pm 0.21$ . It should be noted that the statistics in this area are poor (we have only 36 GMCs). This fact is also emphasized by the very high error on  $N$ .

Finally, the regions with the highest  $\Sigma_{SFR}$  are the spiral arms, the core and the intra-arm regions, where these values reach  $\sim 10 M_{\odot}/yr/kpc^2$ .

Our results are consistent with previous work on this galaxy, as well as other samples of similar galaxies, both in terms of cloud mass and the slope of the KS relations. However, we identify slightly more than half of the GMCs that Rosolowsky identifies, with 4 clouds that we identify having masses larger than theirs. These different results show that our GMC identification method (in which we use the 0-moment and not the velocity cube) is less accurate (as confirmed by the different total masses obtained from the integrated intensity and from the sum of all masses of the identified GMCs,  $(8.1 \pm 0.3) \times 10^8 M_{\odot}$ ).

The KS we get in the bar and bar ends are flatter than those we find in the literature: in the bar, the  $N$  index we obtained is about 30% of that obtained by Querejeta. Whereas that in the bar ends is one tenth part. It must be pointed out that Querejeta treats the bar as one, without distinguishing the ends of the bar.

The methodology adopted in this thesis has been applied in several galaxies and on larger samples of galaxies. In recent years, PHANGS, with the implementation of high resolution observations in the radio and infrared bands, the adoption of more precise methods for detecting GMCs, and the dynamical study of these structures in their respective environments, have provided a better understanding of the link between the properties of GMCs, the mechanisms of star formation, and environmental properties. However, most PHANGS publications are based on observations of the CO(2-1), which provides better resolution (due to the slightly higher frequency), but there is no direct conversion factor between the intensity of this line and the molecular gas. So, the molecular gas mass is often inferred from the CO(2-1) luminosity by assuming a constant  $R_{12*} = CO(2-1)/CO(1-0)$  line ratio. In this sense, observations of the CO(1-0) emission lines are extremely important, since they can provide a direct measure of the  $R_{21}$  value. In fact, the same data we have analyzed have been used in a recent paper [9] to determine  $R_{21}$  in different galaxy regions.

Furthermore, while our work has primarily focused on characterizing GMCs in terms of SFR, there is ample room to further explore their dynamic properties from CO(1-0) line emission. Analyzing virial mass, virial parameter, and proper motions of GMCs could provide a more comprehensive understanding of the dynamic processes governing these molecular structures (as done in [54]). Extending this research to dynamic details could reveal crucial aspects of the star formation cycle and the role of GMCs in different galactic environments, contributing to the ongoing progress in our understanding of molecular structures and key processes in galaxies.

# Bibliography

- [1] Junichi Baba, Kana Morokuma-Matsui **and** Takayuki R Saitoh. “Eventful evolution of giant molecular clouds in dynamically evolving spiral arms”. **in***Monthly Notices of the Royal Astronomical Society*: 464.1 (2017), **pages** 246–263.
- [2] Javier Ballesteros-Paredes **and others**. “From diffuse gas to dense molecular cloud cores”. **in***Space Science Reviews*: 216 (2020), **pages** 1–58.
- [3] Javier Ballesteros-Paredes **and others**. “Molecular cloud turbulence and star formation”. **in***arXiv preprint astro-ph/0603357*: (2006).
- [4] J Bally **and others**. “Herschel observations of the W43 “mini-starburst””. **in***Astronomy & Astrophysics*: 518 (2010), **page** L90.
- [5] Ben Bean **and others**. “CASA, Common Astronomy Software Applications for Radio Astronomy”. **in***Publications of the Astronomical Society of the Pacific*: 134.1041 (2022), **page** 114501.
- [6] H Beuther **and others**. “Interactions of the Galactic bar and spiral arm in NGC 3627”. **in***Astronomy & Astrophysics*: 597 (2017), A85.
- [7] Alberto D Bolatto, Mark Wolfire **and** Adam K Leroy. “The CO-to-H<sub>2</sub> conversion factor”. **in***Annual Review of Astronomy and Astrophysics*: 51 (2013), **pages** 207–268.
- [8] Jakob S den Brok **and others**. “Wide-field CO isotopologue emission and the CO-to-H<sub>2</sub> factor across the nearby spiral galaxy M101”. **in***arXiv preprint arXiv:2302.03044*: (2023).
- [9] JS den Brok **and others**. “Resolved low-J 12CO excitation at 190 parsec resolution across NGC 2903 and NGC 3627”. **in***Monthly Notices of the Royal Astronomical Society*: 526.4 (2023), **pages** 6347–6363.
- [10] Daniela Calzetti. “Star formation rate indicators”. **in***Secular Evolution of Galaxies*: 419 (2013).
- [11] Laurent Chemin **and others**. “An H $\alpha$  study of the kinematics of NGC 3627”. **in***Astronomy & Astrophysics*: 405.1 (2003), **pages** 89–97.
- [12] Mélanie Chevance **and others**. “The molecular cloud lifecycle”. **in***Space Science Reviews*: 216 (2020), **pages** 1–42.
- [13] Laura Chomiuk **and** Matthew S Povich. “Toward a unification of star formation rate determinations in the Milky Way and other galaxies”. **in***The Astronomical Journal*: 142.6 (2011), **page** 197.
- [14] Dario Colombo **and others**. “The PdBI Arcsecond Whirlpool Survey (PAWS): environmental dependence of giant molecular cloud properties in M51”. **in***The Astrophysical Journal*: 784.1 (2014), **page** 3.
- [15] PC Cortes **and others**. “Alma technical handbook”. **in***ALMA Doc*: 9 (2020), **page** 17.
- [16] Donald P Cox. “The three-phase interstellar medium revisited”. **in***Annu. Rev. Astron. Astrophys.*: 43 (2005), **pages** 337–385.

- [17] Timothy A Davis **and others**. “The ATLAS3D Project—XIV. The extent and kinematics of the molecular gas in early-type galaxies”. *in Monthly Notices of the Royal Astronomical Society*: 429.1 (2013), **pages** 534–555.
- [18] Clare L Dobbs **and others**. “Formation of molecular clouds and global conditions for star formation”. *in Protostars and Planets VI*: 1312 (2014), **pages** 3–26.
- [19] Bruce T Draine. *Physics of the interstellar and intergalactic medium*. **volume** 19. Princeton University Press, 2010.
- [20] BG Elmegreen. “Starbursts by gravitational collapse in the inner Lindblad resonance rings of galaxies”. *in Astrophysical Journal, Part 2-Letters (ISSN 0004-637X)*, vol. 425, no. 2, p. L73-L76: 425 (1994), **pages** L73–L76.
- [21] Eric Emsellem **and others**. “The PHANGS-MUSE survey-Probing the chemo-dynamical evolution of disc galaxies”. *in Astronomy & Astrophysics*: 659 (2022), A191.
- [22] ESA/Webb. *weic2403n*. Accessed on: 02/20/2024. 2024. URL: <https://esawebb.org/images/weic2403n/>.
- [23] Yusuke Fujimoto **and others**. “Do giant molecular clouds care about the galactic structure?” *in Monthly Notices of the Royal Astronomical Society*: 439.1 (february 2014), **pages** 936–953. ISSN: 0035-8711. DOI: 10.1093/mnras/stu014. eprint: <https://academic.oup.com/mnras/article-pdf/439/1/936/5617459/stu014.pdf>. URL: <https://doi.org/10.1093/mnras/stu014>.
- [24] P Gratier **and others**. “Molecular and atomic gas in the Local Group galaxy M 33”. *in Astronomy & Astrophysics*: 522 (2010), A3.
- [25] Akihiko Hirota **and others**. “ALMA 12CO (J = 1–0) imaging of the nearby galaxy M83: Variations in the efficiency of star formation in giant molecular clouds”. *in Publications of the Astronomical Society of Japan*: 70.4 (june 2018). 73. ISSN: 0004-6264. DOI: 10.1093/pasj/psy071. eprint: <https://academic.oup.com/pasj/article-pdf/70/4/73/25439343/psy071.pdf>. URL: <https://doi.org/10.1093/pasj/psy071>.
- [26] Luis C Ho, Alexei V Filippenko **and** Wallace LW Sargent. “The influence of bars on nuclear activity”. *in The Astrophysical Journal*: 487.2 (1997), **page** 591.
- [27] Annie Hughes **and others**. “A comparative study of giant molecular clouds in M51, M33, and the Large Magellanic Cloud”. *in The Astrophysical Journal*: 779.1 (2013), **page** 46.
- [28] PA James **and** SM Percival. “Star formation suppression and bar ages in nearby barred galaxies”. *in Monthly Notices of the Royal Astronomical Society*: 474.3 (2018), **pages** 3101–3109.
- [29] Robert C Kennicutt Jr. “Star formation in galaxies along the Hubble sequence”. *in Annual Review of Astronomy and Astrophysics*: 36.1 (1998), **pages** 189–231.
- [30] Robert C Kennicutt Jr. “The global Schmidt law in star-forming galaxies”. *in The astrophysical journal*: 498.2 (1998), **page** 541.
- [31] Robert C Kennicutt Jr **and** Neal J Evans. “Star formation in the Milky Way and nearby galaxies”. *in Annual Review of Astronomy and Astrophysics*: 50 (2012), **pages** 531–608.
- [32] Jaeyeon Kim **and others**. “Environmental dependence of the molecular cloud lifecycle in 54 main-sequence galaxies”. *in Monthly Notices of the Royal Astronomical Society*: 516.2 (august 2022), **pages** 3006–3028. ISSN: 0035-8711. DOI: 10.1093/mnras/stac2339. eprint: <https://academic.oup.com/mnras/article-pdf/516/2/3006/45845229/stac2339.pdf>. URL: <https://doi.org/10.1093/mnras/stac2339>.

- [33] JM Diederik Kruijssen **and others**. “Fast and inefficient star formation due to short-lived molecular clouds and rapid feedback”. in *Nature*: 569.7757 (2019), **pages** 519–522.
- [34] Charles J. Lada **and others**. “STAR FORMATION RATES IN MOLECULAR CLOUDS AND THE NATURE OF THE EXTRAGALACTIC SCALING RELATIONS”. in *The Astrophysical Journal*: 745.2 (january 2012), **page** 190. DOI: 10.1088/0004-637X/745/2/190. URL: <https://dx.doi.org/10.1088/0004-637X/745/2/190>.
- [35] Richard B Larson. “Turbulence and star formation in molecular clouds”. in *Monthly Notices of the Royal Astronomical Society*: 194.4 (1981), **pages** 809–826.
- [36] Myung Gyoon Lee **and** In Sung Jang. “The Tip of the Red Giant Branch Distances to Type Ia Supernova Host Galaxies. II. M66 and M96 in the Leo I Group”. in *The Astrophysical Journal*: 773.1 (2013), **page** 13.
- [37] Mordecai-Mark Mac Low **and** Ralf S Klessen. “Control of star formation by supersonic turbulence”. in *Reviews of modern physics*: 76.1 (2004), **page** 125.
- [38] Piero Madau **and** Avery Meiksin. “The He II Lyman-alpha opacity of the universe”. in *The Astrophysical Journal*: 433 (1994), **pages** L53–L56.
- [39] Barry F Madore. “Numerical simulations of the rate of star formation in external galaxies”. in *Monthly Notices of the Royal Astronomical Society*: 178.1 (1977), **pages** 1–9.
- [40] Christopher F McKee **and** Eve C Ostriker. “Theory of star formation”. in *Annu. Rev. Astron. Astrophys.*: 45 (2007), **pages** 565–687.
- [41] Christopher F McKee **and** Jeremiah P Ostriker. “A theory of the interstellar medium—Three components regulated by supernova explosions in an inhomogeneous substrate”. in *The Astrophysical Journal*: 218 (1977), **pages** 148–169.
- [42] Jennifer Donovan Meyer **and others**. “Resolved giant molecular clouds in nearby spiral galaxies: insights from the CANON CO (1–0) survey”. in *The Astrophysical Journal*: 772.2 (2013), **page** 107.
- [43] Frederique Motte, Peter Schilke **and** Darek C Lis. “From massive protostars to a giant H ii region: submillimeter imaging of the Galactic ministarburst W43”. in *The Astrophysical Journal*: 582.1 (2003), **page** 277.
- [44] Eric J Murphy **and others**. “Microwave continuum emission and dense gas tracers in NGC 3627: Combining Jansky VLA and ALMA observations”. in *The Astrophysical Journal*: 813.2 (2015), **page** 118.
- [45] National Radio Astronomy Observatory. *Basics of Interferometry*. Accesso: 21 novembre 2023. 2019. URL: <https://science.nrao.edu/facilities/alma/naasc-workshops/nrao-cd-spf1/BasicsInterf.pdf>.
- [46] Sachiko Onodera **and others**. “Breakdown of Kennicutt–Schmidt law at giant molecular cloud scales in M33”. in *The Astrophysical Journal Letters*: 722.2 (2010), **page** L127.
- [47] Hsi-An Pan **and others**. “The Gas–Star Formation Cycle in Nearby Star-forming Galaxies. II. Resolved Distributions of CO and H $\alpha$  Emission for 49 PHANGS Galaxies”. in *The Astrophysical Journal*: 927.1 (2022), **page** 9.
- [48] Ismael Pessa **and others**. “Star formation scaling relations at 100 pc from PHANGS: Impact of completeness and spatial scale”. in *Astronomy & Astrophysics*: 650 (2021), A134.
- [49] M Querejeta **and others**. “Stellar structures, molecular gas, and star formation across the PHANGS sample of nearby galaxies”. in *Astronomy & Astrophysics*: 656 (2021), A133.

- [50] Sarah Ragan **and others**. “The Earliest Phases of Star Formation (EPoS): a Herschel key program-The precursors to high-mass stars and clusters”. *in* *Astronomy & Astrophysics*: 547 (2012), A49.
- [51] Thomas Robitaille **and others**. “astrodendro: Astronomical data dendrogram creator”. *in* *Astrophysics Source Code Library*: (2019), ascl-1907.
- [52] Thomas Robitaille **and others**. *Astronomical Dendrograms in Python*. Accesso il: Data di Accesso. 2013. URL: <https://dendrograms.readthedocs.io/en/stable/>.
- [53] Thomas Robitaille **and others**. *Dendrogram Algorithm*. <https://dendrograms.readthedocs.io/en/stable/algorithm.html>. Imagen extraída de: [https://dendrograms.readthedocs.io/en/stable/\\_images/min\\_value\\_final.png](https://dendrograms.readthedocs.io/en/stable/_images/min_value_final.png). 2013.
- [54] Erik Rosolowsky **and others**. “Giant molecular cloud catalogues for PHANGS-ALMA: methods and initial results”. *in* *Monthly Notices of the Royal Astronomical Society*: 502.1 (2021), **pages** 1218–1245.
- [55] Amélie Saintonge **and** Barbara Catinella. “The cold interstellar medium of galaxies in the Local Universe”. *in* *Annual Review of Astronomy and Astrophysics*: 60 (2022), **pages** 319–361.
- [56] Eva Schinnerer **and others**. “The Gas–Star Formation Cycle in Nearby Star-forming Galaxies. I. Assessment of Multi-scale Variations”. *in* *The Astrophysical Journal*: 887.1 (2019), **page** 49.
- [57] Eva Schinnerer **and others**. “The PdBI Arcsecond Whirlpool Survey (PAWS). I. A cloud-scale/multi-wavelength view of the interstellar medium in a grand-design spiral galaxy”. *in* *The Astrophysical Journal*: 779.1 (2013), **page** 42.
- [58] Paul R Shapiro **and** George B Field. “Consequences of a new hot component of the interstellar medium”. *in* *Astrophysical Journal, Vol. 205, pp. 762-765 (1976)*.: 205 (1976), **pages** 762–765.
- [59] Jiayi Sun **and others**. “Cloud-scale molecular gas properties in 15 nearby galaxies”. *in* *The Astrophysical Journal*: 860.2 (2018), **page** 172.
- [60] Jiayi Sun **and others**. “Molecular Gas Properties on Cloud Scales across the Local Star-forming Galaxy Population”. *in* *The Astrophysical Journal Letters*: 901.1 (**september** 2020), **page** L8. DOI: 10.3847/2041-8213/abb3be. URL: <https://dx.doi.org/10.3847/2041-8213/abb3be>.
- [61] Jiayi Sun **and others**. “Star Formation Laws and Efficiencies across 80 Nearby Galaxies”. *in* *The Astrophysical Journal Letters*: 945.2 (2023), **page** L19.
- [62] Yoshimasa Watanabe **and others**. “A 3 mm spectral line survey toward the barred spiral galaxy NGC 3627”. *in* *The Astrophysical Journal Supplement Series*: 242.2 (2019), **page** 26.
- [63] Jonathan P Williams, Leo Blitz **and** Christopher F McKee. “The structure and evolution of molecular clouds: from clumps to cores to the IMF”. *in* *arXiv preprint astro-ph/9902246*: (1999).
- [64] Thomas G Williams, Walter K Gear **and** Matthew WL Smith. “The star formation law at GMC scales in M33, the Triangulum galaxy”. *in* *Monthly Notices of the Royal Astronomical Society*: 479.1 (2018), **pages** 297–314.
- [65] Jingwen Wu **and others**. “Connecting dense gas tracers of star formation in our galaxy to high-z star formation”. *in* *The Astrophysical Journal*: 635.2 (2005), **page** L173.
- [66] Antoine Zakardjian **and others**. “The impact of HII regions on Giant Molecular Cloud properties in nearby galaxies sampled by PHANGS ALMA and MUSE”. *in* *arXiv preprint arXiv:2305.03650*: (2023).

- [67] Dennis Zaritsky, Robert C Kennicutt Jr **and** John P Huchra. “H II regions and the abundance properties of spiral galaxies”. **in** *The Astrophysical Journal*: 420 (1994), **pages** 87–109.